Journal of Structural Geology 211 (2026) 105782

Contents lists available at ScienceDirect

Journal of Structural Geology

journal homepage: www.elsevier.com/locate/sg

A century after Griffith: Towards a combined non-linear criterion for brittle failure

R. Úcar [a], L. Arlegui [b],*, N. Belandria [a,b], J.L. Simón [b]

[a] Universidad de los Andes, Escuela de Ingeniería Geológica, Dpto. de Geomecánica, Mérida, Venezuela
[b] Universidad de Zaragoza, Facultad de Ciencias, Dpto. de Ciencias de la Tierra, Zaragoza, 50009, Spain

ARTICLE INFO

Keywords:
Rock failure criterion
Griffith's criterion
Brittle deformation
Non-linear failure criteria
Numerical simulations

ABSTRACT

A century after Griffith's pioneering work on fracture mechanics, the classical Griffith criterion continues to inform the understanding of tensile failure in brittle materials. However, its predictive capacity under compressive stress conditions remains limited, often underestimating rock strength. This study proposes a revised formulation of the original Griffith criterion — the new Griffith Criterion —that addresses these limitations by introducing a non-linear expression in the tensile and transitional domains. In parallel, a previously published non-linear failure criterion — Úcar's Criterion — is adopted to describe the compressive regime. The two criteria are then analytically combined into a virtually continuous failure envelope that spans the entire range of principal stress conditions. The combined formulation requires only the uniaxial compressive strength and tensile strength as input parameters. From these, all relevant components of the failure envelope are derived, either through closed-form expressions or through strongly correlated empirical relationships. The resulting envelope shows excellent agreement with published triaxial and confined extension test data across a variety of lithologies, accurately capturing the shape and extent of failure in both Mohr and principal stress spaces. The combined criterion is applied to model fracture occurrence in two illustrative scenarios: a sedimentary sequence submitted to tectonic extension and a deep geothermal reservoir subject to thermal stimulation. These examples highlight the predictive potential and practical utility of this approach, particularly when laboratory data are limited. The proposed formulation offers a coherent, computationally efficient alternative to existing empirical criteria for brittle failure in rocks.

1. Introduction

1.1. Context and scope

At the beginning of the 1920s, the British engineer Alan Arnold Griffith (1893–1963) published his theory on the formation of macroscopic fractures. Griffith (1921, 1924) described the behaviour of crack propagation for a flat elliptical crack (chosen for mathematical simplicity) by considering the energy involved. Essentially, Griffith characterised crack propagation in terms of the internal energy of the system relative to the increase in crack length. The fracture is initiated as a consequence of tensile failure induced by stress concentrations at the tips of pre-existing microcracks (nowadays known as Griffith micro-cracks) in the material. The theory accurately predicts that the microcracks most likely to grow and generate macroscopic fractures are those orientated perpendicularly to the minor principal stress axis, σ_3, in accordance with experimental observations.

These studies laid the foundations for the present understanding of fracture phenomena in brittle materials across a wide range of fields, including rock mechanics. This contribution was, without a doubt, revolutionary, as it elevated practice in such disparate fields as aeronautical engineering and structural geology to a new level. However, it was not without flaws, since when compared with experimental data — although in many respects the observations confirm the theory (Tang and Hudson, 2010) — discrepancies with the predictions were observed. Specifically, the theoretical results of Griffith (1924) indicate that, in an isotropic material containing microcracks with random orientations, fractures will occur provided that the following condition is met between the effective principal stresses, σ_1 and σ_3, and the tensile strength, T_0 (with a negative value)[1]:

$$(\sigma_1 - \sigma_3)^2 = -8 \cdot T_0 \cdot (\sigma_1 + \sigma_3) \tag{1}$$

where T_0 is the tensile strength of the rock.

* Corresponding author.
E-mail addresses: robertoucar@gmail.com (R. Úcar), arlegui@unizar.es (L. Arlegui), norlyb@gmail.com (N. Belandria), jsimon@unizar.es (J.L. Simón).

[1] In this work, unless otherwise stated, all stresses are to be considered effective. Also, we will follow the usual convention in structural geology of considering compressive stresses as positive, and tensile as negative.

https://doi.org/10.1016/j.jsg.2026.105782
Received 12 March 2026; Received in revised form 13 August 2026; Accepted 15 August 2026
Available online 24 August 2026

If we consider the boundary conditions of the uniaxial compression test, or simple compression test, where $\sigma_3 = 0$, it follows that the uniaxial compressive strength $C_0 = -8 \cdot T_0$ (that is equivalent to writing $C_0 = 8 \cdot |T_0|$), but reviews of experimental results reveal that this is not always the case (Pollard and Fletcher, 2005, for instance).

The greatest predictive success of Griffith's theory is observed in the domain of negative normal stresses (the tensile regime), whereas, in the compressive region, it systematically underestimates the strength of the materials. This led to the consideration of friction within the microcracks as an additional factor (since they tend to close under compression), ultimately resulting in distinct proposals of combined failure criteria encompassing the full spectrum of stress settings, expressed in the corresponding envelopes within the (σ, τ) space. Some of such proposals are:

i. prolongation of the Griffith parabolic envelope (equation by Murrell, 1958) into the compressive region;
ii. combination of the Griffith curve with the Coulomb straight line to build the so-named "Modified Griffith Criterion" (Brace, 1960; McClintock and Walsh, 1962);
iii. hypothetical extension of the Mohr–Coulomb empirical envelope into the tensile region, an option earlier ruled out by Leon (1934) (in Nadai, 1950).

Although the combined criterion Griffith–Coulomb could be considered to be in good health — given its presence in modern publications (Anderson, 1951; Fossen, 2010; Schultz, 2019; Peacock et al., 2021, 2024) — derivation and use of linear failure criteria have been the subject of extensive debate and robust empirical evidence has led to a preference for a non-linear criterion in the compressive domain (Reeher et al., 2023). It is worth noting that numerous empirical, non-linear criteria exist which, with varying degrees of success, are capable of describing the failure behaviour of rocks: Drucker and Prager (1952), Fairhurst (1964), Murrell (1965), Mogi (1967), Bieniawski (1974) — a notably sound modification of Murrell's criterion — and Hoek and Brown (1980, 2019), which continues to dominate almost entirely within the field of rock engineering.

Recently, Úcar (2021) proposed a non-linear failure criterion derived from the mathematical procedures to determine the equation of the envelope of a family of curves. Based on uniaxial compressive and tensile strength data — and thus grounded in experimental evidence — this criterion, when applied through the resulting theoretical equations, yields excellent results (Cordón et al., 2024; Úcar et al., 2024).

In this work, we revisit Griffith's equations with the aim of addressing the difficulties in connecting them with non-linear failure criteria in the compressive regime. As a result, we will propose a new Griffith criterion (NGC) whose potential compatibility with Úcar's criterion for the compressive domain will be examined. Beyond the contribution it may make in the field of fracture mechanics, we intend for this paper to be of interest to a general audience of structural geologists. In this way, it will contribute to refining the models of relationships between (i) the geometry and kinematics of fracture systems in nature, and (ii) the stress systems responsible for their formation, helping to discern the usefulness of the different fracture types in palaeostress analysis. Moreover, we will test the usefulness of the failure model proposed by means of geological examples.

1.2. The challenge of an integrated theory of rock failure: a historical overview

Traditionally, three modes of fracture have been distinguished, based mainly on kinematic criteria, which in turn can be linked to distinct loading settings: Mode I, Mode II, and Mode III (Irwin, 1963). Mode I fractures are pure tensile fractures, formed under a σ_3 stress axis orthogonal to the plane in which they propagate. They are, as we have seen, more or less satisfactorily explained by Griffith's theory (Griffith, 1921, 1924). Mode II are shear fractures, that form under an oblique compressive stress, at an angle (α) with σ_1 that depends on the angle of internal friction of the rock (φ). They were explained within the framework of the Mohr–Coulomb frictional criterion, which gave rise to the conjugate fault model (Anderson, 1951). Mode III fractures are rare; in principle, they require the application of torsional loading that is difficult to envisage in natural tectonic stress fields. That loading path could be present close to fault tips or along-strike relays between normal or reverse faults (Schultz, 2019), or represent local anomalies at the propagation front of tensile joints, as suggested by the geometry of fringe joints associated with plumose marks (Simón et al., 2006).

Leaving Mode III aside, the true basic fracture modes are Mode I and Mode II, which some authors have considered as strictly separated "fracture realms", subject to different mechanical laws (e.g., Pollard and Aydin, 1988; Engelder, 1999). That view implies that

i. there is no universal failure criterion for predicting the angle of faulting in the tensile field (Engelder, 1999);
ii. there is no "intermediate" or transitional failure mode between both of them; or even,
iii. the concept of shear joint itself is nonsense (Pollard and Aydin, 1988).

However, for decades, most authors have considered that extension and shear fractures represent end-members of a continuous range of fracture types, either reasoning positively in favour of a continuous transition from tensile to shear fracture, i.e., the existence of hybrid, tensile-shear fractures (e.g., Muehlberger, 1961; Hoek, 1965; Hancock, 1985; Price and Cosgrove, 1990; Ramsey and Chester, 2004; Belayneh and Cosgrove, 2010; Lan et al., 2019), or assuming it explicitly or implicitly (e.g., Mattauer, 1973; Hobbs and Means, 1976; Etheridge, 1983; Suppe, 1985; Davis et al., 2011; Sibson, 1998; Fossen, 2010; Ferrill et al., 2012; Schultz, 2019; Peacock et al., 2021; Reeher et al., 2023). All of them consider, in practice, a composite failure criterion, combining the Mohr–Coulomb envelope for shear fracture under compressive stresses with a parabolic Griffith envelope for tensile/hybrid fracture under tensile stresses.

Scepticism regarding the actual existence of a "transitional fracture realm" likely stems from the ambiguous nature of observations documenting hybrid or transitional fractures between Mode I and Mode II loading, coupled with the inconclusive nature of many experimental demonstrations of their occurrence. A critical parameter for testing the hypothesis of transitional or hybrid fracture is the angle α between σ_1 and the fracture plane. Mode I fractures are orthogonal to σ_3 and parallel to σ_1 ($\alpha = 0$), while shear fractures in compressive settings show $\alpha = 45° - \varphi/2$. Given that, under low to moderate confining pressure, φ usually lies between 30° and 40°, α typically ranges from 25° to 30°. Within this framework, field evidence of hybrid fracture is represented by:

i. pairs of joint sets, with evidence of being conjugate systems, that show low or very small dihedral angles (2α in the range of $10 - 45°$);
ii. "joint spectra", i.e., joint ensembles exhibiting a continuum of directions symmetrically distributed at low angles around the σ_1 axis (Hancock, 1985, 1986; Hancock and Engelder, 1989; Simón et al., 1999; Arlegui and Simón, 2001).

But not much literature exists in support of the relationships between such joints and stress systems. Concerning the experimental approach, confined extension tests have produced fracture sets consistent with the hybrid failure mode, but they have been unsuccessful at predicting fracture orientation: although the dihedral angles observed become systematically smaller as confining pressure decreases (Muehlberger, 1961; Ramsey and Chester, 2004), they are also systematically smaller than those predicted by the parabolic envelope

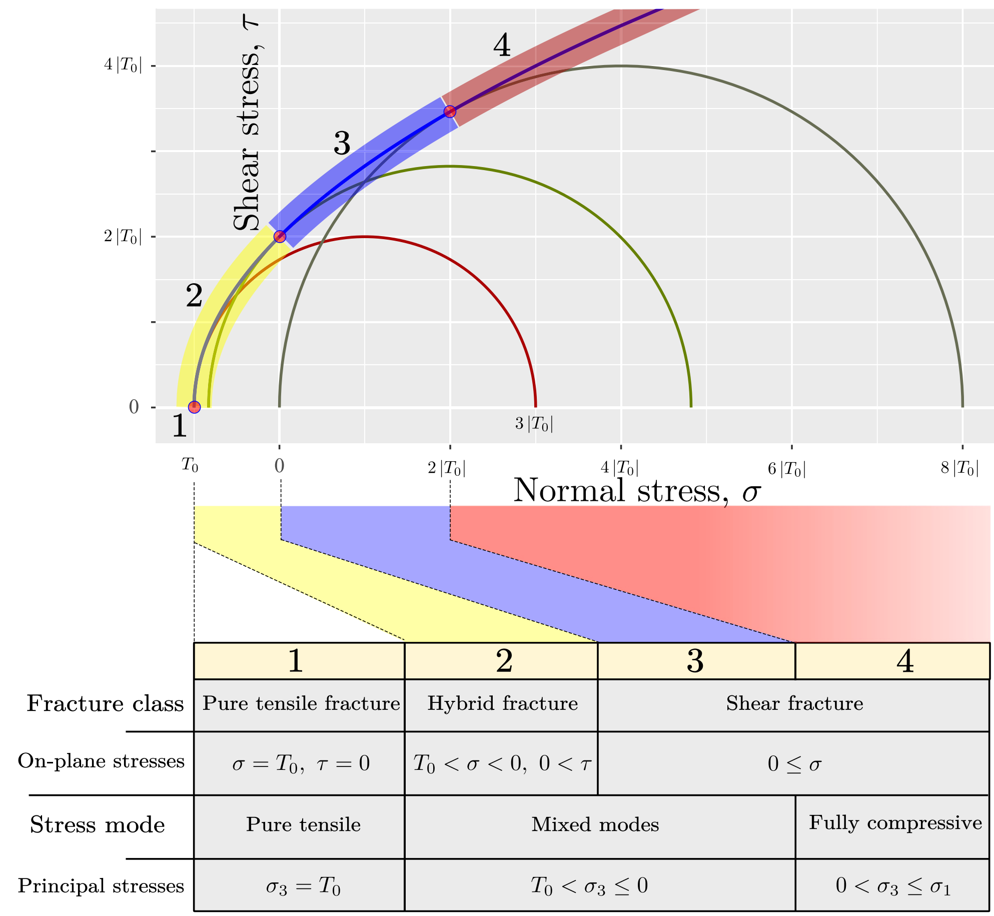

Fig. 1. Proposed delineation of regions within the failure envelope, aimed at clarifying the terminology used when referring to hybrid fractures and their associated stress states. Further explanation is provided in the main text.

extrapolated over the tensile stress regime (Brace, 1964; Engelder, 1999; Ramsey and Chester, 2004; Bobich, 2005).

In spite of such inconclusive results, since the 60's, the notion that there is no mechanical decoupling between tensile and shear failure processes is firmly established in the scientific literature, including most structural geology textbooks. As an operational tool, a single parabolic envelope covering all stress conditions from pure tensile to compressive under high confining pressure is used worldwide for analysing the conditions of macroscopic failure and the geometry of the resulting fracture systems. Nevertheless, it is true that a unified failure theory that integrates or combines Griffith and Mohr–Coulomb theories has yet to be found.

Considerable effort has been made for one century in pursuit of such a connection, starting with Griffith himself. His theory provides a useful basis for understanding fracture initiation and coalescence (Hoek and Martin, 2014), and justifies the existence of hybrid fractures. Its basic equation, initially defined — Eq. (1) — in the (σ_3, σ_1) space, can also be expressed by a parabola when it is translated into the (σ, τ) space (Murrell, 1958):

$$\tau^2 + 4\ \mathrm{T}_0\sigma - 4\ \mathrm{T}_0^2 = 0 \tag{2}$$

Writing τ as a function of σ and expressed in dimensionless form with respect to $|T_0|$:

$$\frac{\tau}{|T_0|} = 2\sqrt{1 + \frac{\sigma}{|T_0|}} \tag{3}$$

From this equation, it can be inferred:

i. A relationship between cohesion c and tensile strength T_0: $c = 2 \cdot |T_0|$, since $c = \tau$ when $\sigma = 0$.
ii. The angle of inclination of the curve at the point $\sigma = 0$ is 45°, since the first derivative of Eq. (3) with respect to σ is equal to 1 at that point.

In principle, Griffith's theory was formulated for the tensile stress region ($\sigma < 0$); the corresponding parabola extends from $\sigma_{(\tau=0)} = T_0$ to $\sigma_{(\tau=2|T_0|)} = 0$ (segment 2 in Fig. 1) and, therefore, represents failure planes supporting a shear component and belonging to the category of hybrid fractures. Since Griffith's curve makes an angle of 45° with the σ axis where it crosses the τ axis, fractures represented by this point have $\alpha = 45° - (45°/2) = 22.5°$. Therefore, Griffith can explain pure Mode I fractures ($\alpha = 0$, point 1 in Fig. 1) and hybrid fractures with $0 < \alpha < 22.5°$ (segment 2 in Fig. 1).

Let us move to the right of the ordinate axis, where the Mohr–Coulomb frictional criterion is often accepted as the standard model. However, strictly speaking, a Mohr–Coulomb envelope based on experimental data can only be defined at segment 4 of Fig. 1, beyond the point representing the uniaxial compression failure test (where $\sigma_1 = C_0$ and $\sigma_3 = 0$). If we adopt a linear strength relationship, the coordinates (σ, τ) of that point would be: $\sigma = (\sigma_1)/2 \cdot (1 - \sin\varphi)$; $\tau = (\sigma_1)/2 \cdot \cos\varphi$. In the case of $\varphi = 30°$, $\sigma = 0.25 \cdot C_0$; $\tau = \sqrt{3}/4 \cdot C_0 = 0.433 \cdot C_0$; normalised to the absolute value of tensile strength: $\sigma = 2|T_0|$; $\tau = 3.46|T_0|$. From that point to the left, the Mohr–Coulomb envelope does not apply. Segment

3 of Fig. 1 graphically represents the apparent gap between true tensile and compressive failure stress conditions.

In this respect, we would like to clarify a terminological ambiguity that persists in the literature. We refer to the confusing application of the term "hybrid", not to the fracture itself ("hybrid tensile-shear fracture", mixed Mode I + Mode II), but to the stress regime at failure (mixed tensile and compressive stress states: $\sigma_3 < 0$; $\sigma_1 > 0$; (e.g., Ramsey and Chester, 2004).

According to that notion:

i. Pure tensile fractures are those formed when subjected to $(\sigma_1 - \sigma_3) \leq 4|T_0|$ (point 1 in Fig. 1).
ii. Compression fractures are those formed under $(\sigma_1 - \sigma_3) \geq 8|T_0|$ (segment 4 in Fig. 1).
iii. Hybrid fractures are those formed within the range bounded by these two extremes: $4|T_0| < (\sigma_1 - \sigma_3) < 8|T_0|$ (segments 2 and 3 in Fig. 1). In particular, this includes the case when $(\sigma_1 - \sigma_3) = 4\sqrt{2}|T_0|$, which results in failure on a plane with $\sigma = 0, \tau = 2|T_0|$.

This confusing correspondence between stress settings and fracture modes gives rise to a contradiction: some of the fractures in the stress scenario (iii) undergo $\sigma > 0$; no tensile component acts on them and, therefore, they cannot be considered "hybrid" but rather shear fractures s.s. In order to resolve such confusion, Hancock (1985) made a useful distinction between two subdomains within the domain of "mixed stress states", then assumed by other authors (e.g., Price and Cosgrove, 1990):

a. That with $4 \cdot |T_0| < (\sigma_1 - \sigma_3) < 5.66 \cdot |T_0|$, where both σ_3 and the σ component supported by the failure plane are negative: Hybrid fractures s.s. form in these conditions, their planes making angles with σ_1 in the range $0 < \alpha < 22.5°$.
b. That with $5.66 \cdot |T_0| < (\sigma_1 - \sigma_3) < 8 \cdot |T_0|$, where σ_3 remains negative but the σ component on the plane becomes positive: Shear fractures s.s. form in such settings, making angles α with σ_1 in the range of 22.5° to 30°.

We will strictly use the term "hybrid" for fractures formed under $4 \cdot |T_0| < (\sigma_1 - \sigma_3) < 5.66 \cdot |T_0|$, which can be explained by Griffith's theory (subdomain A; segment 2 in Fig. 1). Subdomain B (segment 3 in Fig. 1) will be the "playing field" where we will try to find the "meeting point" between the former and the Mohr–Coulomb theory in order to construct the combined failure model.

There have been numerous attempts over time to connect the Mohr–Coulomb line with the Griffith curve, "filling the gap" represented by segment 3 in Fig. 1. Simply extrapolating a Coulomb straight line to the left does not work: although such an operation is made for quickly defining the cohesion c at the intersection with the τ axis, it is an arbitrary imposition that it must connect exactly at that point with the Griffith curve. Even if it did coincide numerically, it is almost impossible for the transition to be 'smooth', unless $\varphi = 45°$ (inclination of the Griffith parabola at that point). In a general case, where both failure envelopes join at the τ axis ($\sigma = 0$), there is a discontinuity in their slopes (Peacock et al., 2021). Obviously, nor does it resolve the challenge of unifying failure theories through a simplistic extension of the Mohr–Coulomb failure envelope into the tensile region, as already recognised by Leon (1934; as cited in Nadai, 1950) and later corroborated by Engelder (1999).

In such a situation, it is necessary to explore two other (not mutually exclusive) possibilities: (a) extending Griffith's curve to the compressive domain, or (b) substituting the Coulomb straight line with a non-linear failure criterion in that domain.

Although the Griffith criterion was originally designed for dilatant crack propagation, a remarkable consequence of the theory is that the presence of internal cracks can give rise to tensile stresses large enough for fracture propagation even if a positive normal component acts on it, thus including frictional forces (Griffith, 1924). Two options have been considered:

i. the "natural" prolongation of the Griffith curve, constructed from the equation by Murrell (1958);
ii. the "Modified Griffith Criterion" based on extending the Griffith curve to the right of the τ axis by using the equation $\tau = 2|T_0| + \mu\sigma$ (Brace, 1960; McClintock and Walsh, 1962).

Option (ii) has been frequently embraced in papers and textbooks as a realistic and successful solution that satisfies most experimental data (e.g., Price, 1966; Fossen, 2010; Schultz, 2019). Nevertheless, it represents a simplistic approach that encounters the same problem mentioned above: the impossibility of a "smooth connection" between both portions. Option (i) can provide a better solution, as we next discuss.

The Griffith curve $\tau = \left(-4\ \mathrm{T_0}\sigma + 4\ \mathrm{T_0}^2\right)^{1/2}$ makes an angle of 45° with the σ axis at $\sigma = 0$. Within the compressive stress region, that angle decreases up to 30° at the point with $\sigma = -2 \cdot T_0, \tau = \sqrt{3}/4 \cdot 8 \cdot |T_0| = 3.48 \cdot |T_0|$, i.e., the point where the Mohr circle representing uniaxial compression should be tangent to the curve if the apparent internal friction angle is $\varphi = 30°$. Assuming that the latter represents a realistic value for the internal friction angle, that point could be the first candidate as "meeting point" for merging the macroscopic Griffith criterion with the Mohr–Coulomb criterion. This choice involves that the entire searched "gap" would be covered by the Griffith curve. Another possibility is suggested by Sibson (1998): by adopting a coefficient of internal friction $\mu = 0.75$ ($\varphi = 36.9°$), the "meeting point" would be located at $\sigma = 0.777|T_0|, \tau = 2.666|T_0|$, near the centre of the gap. In reality, both choices are arbitrary, hypothetical solutions not tested empirically. According to the judgement by McCormick and Rutter (2022), the truth is that, assuming that the transitions between failure modes are part of a continuous spectrum, there is no experiment that defines the boundary between failure regions where the different laws of mechanics apply.

Concerning the search for a non-linear relationship in the compressive domain (which could eventually join the Griffith parable at the compression–extension transition domain), the first robust proposal was that by Hoek and Brown (1980). Using the Griffith theory as a starting point, these authors derived an analytical relationship that fitted shear failure laboratory results under triaxial compressive tests. Hoek–Brown failure criterion is the most widely used in engineering applications, but it has been disregarded in favour of the linear Coulomb criterion by structural geologists (Reeher et al., 2023). In our opinion, this is mainly due to the fact that the Hoek–Brown relationship was initially expressed in the (σ_3, σ_1) space, which is not useful for analysing the geometrical connection between fractures and stresses. The original equation was

$$\sigma_1 = \sigma_3 + \sqrt{m \cdot C_0 \cdot \sigma_3 + s \cdot C_0^2} \tag{4}$$

where C_0 is the uniaxial compressive strength of intact rock, and m and s are material parameters. Nevertheless, the Hoek–Brown failure criterion can also be expressed in the (σ, τ) space. The first proposal was due to Hoek (1983), expressed by this equation:

$$\tau = \left(\cot \varphi_i - \cos \varphi_i\right) \cdot \frac{m \cdot C_0}{8} \tag{5}$$

where τ denotes the shear stress at failure, C_0 is the uniaxial compressive strength, and φ_i is the instantaneous friction angle (Hoek, 1983). However, that author did not derive an explicit expression for the normal stress, which was later proposed by Úcar (1986):

$$\tau = \frac{mC_0}{8}\left\{\frac{(1 - \sin \varphi)\left(1 - \sin^2 \varphi\right)^{1/2}}{\sin \varphi}\right\} \tag{6}$$

$$\sigma = \frac{mC_0}{8}\left[\frac{1}{2\sin^2 \varphi} + \sin \varphi\right] - C_0\left(\frac{3m}{16} + \frac{s}{m}\right) \tag{7}$$

The resulting parabolic curve in the (σ, τ) space can predict the angles between fracture surfaces and stress axes using Mohr circles. Such angles will change as a function of the variable angle of instantaneous internal friction φ_i, which in turn depends on the normal stress level at failure (Hoek, 1983):

$$\varphi_i = \arctan\left(4h\cos^2\left(30 + 1/3\arcsin h^{-3/2}\right) - 1\right)^{-1/2} \quad (8)$$

where

$$h = 1 + \frac{16\left(m\sigma + s\sigma_c\right)}{3m^2\sigma_c} \quad (9)$$

Such a relationship is consistent with the systematic variation of fracture angles observed in laboratory tests under distinct differential stress magnitudes (Ramsey and Chester, 2004; McCormick and Rutter, 2022). It is also consistent with field evidence presented by Reeher et al. (2023), who studied conjugate mesoscale fault systems in the Jurassic Moab Tongue sandstone adjacent to the Salt Valley anticline (Utah, US). The authors interpret a release of differential stress close to the soft salt body, driven by its mechanical response to tectonic loading, which results in a systematic decrease in the dihedral angle of conjugate faults as a function of distance to the salt-sediment interface. It is important to note that the fracture surfaces studied do not show any evidence of hybrid-mode failure. This suggests that, for this rock, the non-linear relationship entirely occurs within the compressive domain, i.e., it is independent of the parabolic Griffith envelope for the extensional one.

In short, enormous efforts have been made for decades in order to unify the theory of rock fracturing. Despite all of these efforts, in our opinion, there is still room for improvement in the task of establishing the continuity of fracture processes between tensile and compressive settings, and therefore the coherence of their constitutive laws. The challenge is to explore deeper through a threefold approach:

i. Searching analytically for a composite/mix/combination of curves, i.e. failure laws, that could join as accurately as possible within the "gap" and thus provide a theoretical basis (even if it was not strictly a "unified theory") for the complete tensile-hybrid-shear fracture transition.
ii. Testing the most consistent analytical solution by empirically comparing it with a database of fracture experiments that is as wide as possible.
iii. Ensuring the mechanical significance of such a composite model, which will need to build a reliable scenario of failure and fracture propagation processes at the microscale.

The first two approaches are the focus of the present article, but keep in mind that the third one is an essential requirement for making sense of them. Contributing to observational and experimental evidence on fracture processes at the microscale is outside our scope. Nevertheless, there exists abundant literature about this topic, to the extent that it can respond to the fundamental objections raised by sceptics and provide a solid justification for efforts at theoretical unification. We close this historical review by addressing the main topics in this respect.

Two basic notions should be kept from "sceptical literature". First: Mohr diagrams, Mohr–Coulomb and Griffith envelopes, internal friction angles... do not allow an intimate understanding of the process of fracture initiation, propagation, and arrest (Pollard and Aydin, 1988). They are just tools for describing and predicting the macroscopic geometry (e.g., the dihedral angle of conjugate fault systems) of fracture systems and their relationship with stress axes. Second, linear elastic fracture mechanics does not support the notion that individual cracks propagate in their own plane when subjected to a shear stress component (Engelder, 1999); i.e., macroscopic hybrid tensile-shear fractures, at a small angle α to σ_1, cannot undergo on-plane propagation.

Accepting these two premises does not contradict the attempt to merge the fracture theories. On the contrary, they open the door to an integrated view based on dissociating the essence of Griffith's theory, which deals with the initiation of microscopic tensile cracks, from the subsequent propagation of macroscopic fractures (Brace, 1960; Brace and Bombolakis, 1963; Hoek and Martin, 2014). The key is that fracture surfaces are approximately planar at the sample scale, but complex at the grain scale, developed through the linkage of an array of en-echelon interacting tensile cracks (Ramsey and Chester, 2004). This notion has developed since the 60's, in parallel with theoretical discussions on failure laws, combining more or less intuitive approaches with robust experimental evidence.

Brace and Bombolakis (1963) investigated stress concentration at the tips of cracks from photoelastic experiments. They found that, in uniaxial tension, the maximum tensile stress concentrates at the tip of the crack axis, while in compression the point of maximum tensile stress lies between the long axis and the direction of σ_1. In the first case, crack propagation takes place in its own plane from the tip point. In the second case, either isolated or grouped in an array, cracks grow along a curved path that becomes parallel to σ_1, giving rise to curved branches (referred to as "wing cracks" in recent literature: e.g., Willemse and Pollard, 1998; Pollard and Fletcher, 2005; McCormick and Rutter, 2022). A fault s.s., with an inclination of ≈ 30° to the σ_1 axis, does not result from the growth of a single crack but from the interaction of multiple en-échelon cracks through such branch cracks under increasing applied stress. Such an evolutionary model received crucial support when volume changes observed during triaxial compression tests, preceding the macroscopic rupture, leaded to the notion of dilatancy (Brace et al., 1966). Dilatancy represents an increase in porosity that was early attributed to crack opening; experimental results confirmed that the pattern of crack occurrence correlated with the directionality of dilatancy and with the observed macroscopic stress–strain setting (Scholz, 1968).

Peng and Johnson (1972) and Tapponnier and Brace (1976) observed that shear faulting of specimens submitted to compression is preceded by the development of bands of dense transgranular crack growth. The resulting fault surfaces consist of small staircase-arranged cracks, which are themselves roughly parallel to the σ_1 axis. Reches and Lockner (1994) mapped tensile microcracks from acoustic emission events and observed that during early loading, they occur randomly, without significant interaction between them and without foreshadowing what will be the location and angle of the future fault. According to these authors, the interaction of those microcracks gives rise to a band (process zone) of high density en-échelon microcracks, which spreads into the intact rock. Meanwhile, its central part yields by shear, and an incipient fault forms and propagates in its own plane at an angle of 20 – 30° to σ_1. This model provides a physical basis for the internal friction angle as empirically defined. Reches and Lockner (1994) confirms the analysis by Brace and Bombolakis (1963): under compressive tests, the region of maximum tension induced by an open crack is inclined at an angle α of about 30° with respect to its axis, so that those neighbouring cracks located in that direction will be the most suitable for coalescing and forming the process zone. The angle between the fault plane and σ_1 is empirically controlled by the internal friction angle but ultimately determined at the microscale by the spacing/length ratio of fissures. According to this model, α = 30° can be considered the maximum value, while angles ranging from 30° to nearly 0° can be found under transitional, mixed compressive-tensile stress settings, i.e. in propagation scenarios with crack spacing/length ratio tending to 0.

The essence of such an evolutionary model has also been supported by other authors, either from analytical and photoelastic approaches (Horii and Nemat-Nasser, 1985), from Scanning Electron Microscopic (SEM) mapping (Wibberley et al., 2000), or from actual mesoscale fracture systems in rocks (Segall and Pollard, 1983; Etchecopar et al., 1986). A recent and very clear synthesis is due to McCormick and Rutter (2022). Interestingly, this model is also explicitly suggested by Engelder (1999), as a way to reconcile his critical viewpoint with the almost unanimous aspiration for a unified fracture theory.

1.3. Objectives

The formal objectives of the present work are:

1. Formulating a New Griffith Criterion (NGC) that addresses the perceived discrepancies (see Section 2) between the original Griffith criterion (OGC) and experimental data.
2. Searching analytically for a composite of the NGC curve and the Úcar curve that could join as accurately as possible within that 'gap' at the mixed stress mode. That would involve a combination of failure laws covering the entire range of stress modes and would provide a theoretical basis (even if it was not strictly a 'unified theory') for the complete tensile-hybrid-shear fracture transition.
3. Testing empirically the most consistent analytical solution by comparing it with a database of fracture experiments as wide as possible.
4. Testing the reliability and usefulness of such a composite failure criterion in two geological examples: the development of both pure tensile and hybrid joints under an extensional stress field, and induced thermal fracturing of a rock mass.

2. The original Griffith criterion (OGC)

The principal contribution of Griffith's theory lies in its explanation of why the tensile strength of interatomic bonds in brittle solids is significantly higher than the tensile strength observed at the macroscopic scale. The theoretical tensile strength of brittle rocks is approximately 10% of their elastic modulus (E); however, laboratory results at the macroscopic level typically amount to only about 0.01% of E (Gudmundsson, 2011).

For instance, in the case of strong rocks, the elastic modulus is typically $E \approx 10^5$ MPa, and hence the theoretical tensile strength should be around 10^4 MPa. Yet, in practice, the observed tensile strength is $|T_0| \approx 3$ to 25 MPa.

Undoubtedly, this large discrepancy between the theoretical and observed tensile strength values was Griffith's major contribution, laying the foundations of modern fracture mechanics by establishing a relationship between the stress required to initiate fracture and the size, and shape, of the crack.

Griffith's criterion (OGC) for crack propagation is based on the following principle:

A pre-existing, favourably oriented flaw will propagate when the reduction in elastic strain energy equals or exceeds the energy required to create the new surface area of the crack. In his model, he considered an elliptical flaw or imperfection with a major semi-axis of dimension a and with eccentricity close to unity.

Under these conditions, brittle fracture will occur as a result of the competition between the strain energy released and the surface energy required to create new fracture surfaces. Therefore, crack propagation will take place when the rate of strain energy release equals the rate of surface energy expenditure. In the Supplementary Materials file (section A. The original Griffith Criterion), more details on the energy balance conditions are included.

The application of the above for the case of rocks, leads to the OGC:

$$\left.\begin{array}{ll} \sigma_3 = T_0 & \text{, if: } \sigma_1 \le -3\sigma_3 \\ \left(\sigma_1 - \sigma_3\right)^2 = -8 \cdot T_0 \cdot \left(\sigma_1 + \sigma_3\right) & \text{, if: } \sigma_1 \ge -3\sigma_3 \end{array}\right\} \tag{10}$$

That is, in the pure traction zone, a vertical line (see Fig. 2A, segment $P_0 - P_1$) $\sigma_3 = T_0$, and in the transition regime, the failure criterion is described by a conic section (a parabola).

From the second expression in Eq. (10), it derives that:

$$\frac{\sigma_1}{|T_0|} = \left(\frac{\sigma_3}{|T_0|} + 4\right) + 4\sqrt{1 + \frac{\sigma_3}{|T_0|}} \text{ , for } T_0 \le \sigma_3 \le 0 \tag{11}$$

Therefore, from Eq. (11) when $\sigma_3 = T_0$, then $\sigma_1 = 3\left|T_0\right|$, and, as shown in Fig. 2, point $P_1\left(T_0, 3\left|T_0\right|\right)$ defines the starting point of the failure parabola.

Table 1 summarises the relevant OGC equations under various boundary conditions. Several implications follow, as discussed in the Introduction. Specifically, the OGC predicts that the ratio $C_0/|T_0| = 8$, and that the inclination of the failure envelope at the intersection with the τ axis ($\sigma = 0$) is $\beta = 45°$, and $\beta = 30°$ when $\sigma_3 = 0$.

Based on data compiled from the specialised literature, a total of 186 experimental datasets reporting values of C_0 and T_0 were analysed (see Fig. 3), as documented by Johnston (1985), Cordón et al. (2024), and those included in RocData™v4.2. The histogram shows the highest frequency in the 10–14 range, and the associated kernel density curve peaks near 12. The mean value of the ratio C_0/T_0 across all datasets is 15.65, which almost doubles the theoretical value (8), while the median is 13.82. Furthermore, in the boxplot representation, the reference value $C_0/|T_0| = 8$ lies below the first quartile, indicating that more than 75% of the data fall above this threshold. These observations, together with the nature of the distribution (see Fig. 3), suggest that the use of the Original Griffith Criterion (OGC) with a fixed ratio of $C_0/|T_0| = 8$ may lead to misleading interpretations unless suitable adjustments are applied.

Some progress has been made in addressing the limitations of the Original Griffith Criterion (OGC), beyond the already commented proposal of McClintock and Walsh (1962). In a similar vein, Murrell and Digby (1970) introduced further modifications to account for observed deviations in rock strength behaviour. However, as noted by Baud et al. (2014), such adaptations typically preserve the fundamental assumption of the OGC—namely, that macroscopic failure is governed by the propagation of a single microcrack of critical orientation and size. This assumption is explicitly questioned by Baud and co-authors, who emphasise the pronounced influence of porosity on the uniaxial compressive strength of rocks.

A further notable contribution is the criterion proposed by Castro et al. (2016), which derives from first principles and integrates the Theory of Critical Distances (Taylor, 2008) into the OGC framework. This approach requires either the execution of multiple fracture toughness tests with varying notch radii, in order to identify the critical distance that best fits the experimental data, or alternatively, the performance of two such tests combined with analytical or numerical evaluation of the stress field surrounding the notch tip. As a practical alternative, the required model parameters may be estimated empirically through correlation considering varied strength ratios $C_0/|T_0|$.

3. Úcar's criterion (UC)

Úcar (2021) proposes a new failure criterion for the compressive domain where the principal stresses σ_1 and σ_3 are related by the following equation:

$$\overline{\sigma}_1 = k_1\left(\overline{\sigma}_3 - \xi\right) + k_2\left(\overline{\sigma}_3 - \xi\right)^{1/2} \tag{12}$$

where $\overline{\sigma}_1 = \left(\sigma_1/C_0\right)$, $\overline{\sigma}_3 = \left(\sigma_3/C_0\right)$, k_1 and k_2 are material-dependent constants, and $\xi = \left(\sigma_t/C_0\right)$, or in the notation adopted in this paper, $\xi = \left(T_0/C_0\right)$ (let us remember, tensile stresses are negative).

The nonlinear criterion is expressed as a quadratic equation relating the principal stresses σ_1 and σ_3 at the onset of failure. This formulation enables the determination of the shear strength envelope in rocks and other brittle materials, such as concrete.

The corresponding plane curve is a conic section described by a parabola, which provides a satisfactory approximation of the general behaviour observed in experimental strength data.

Under this empirical criterion for two-dimensional fracture, the normal stress acting on the fracture plane is computed in the initial phase of the analysis by solving a first-order linear differential equation. Once this is achieved, the failure envelope—or intrinsic strength curve—is derived accordingly.

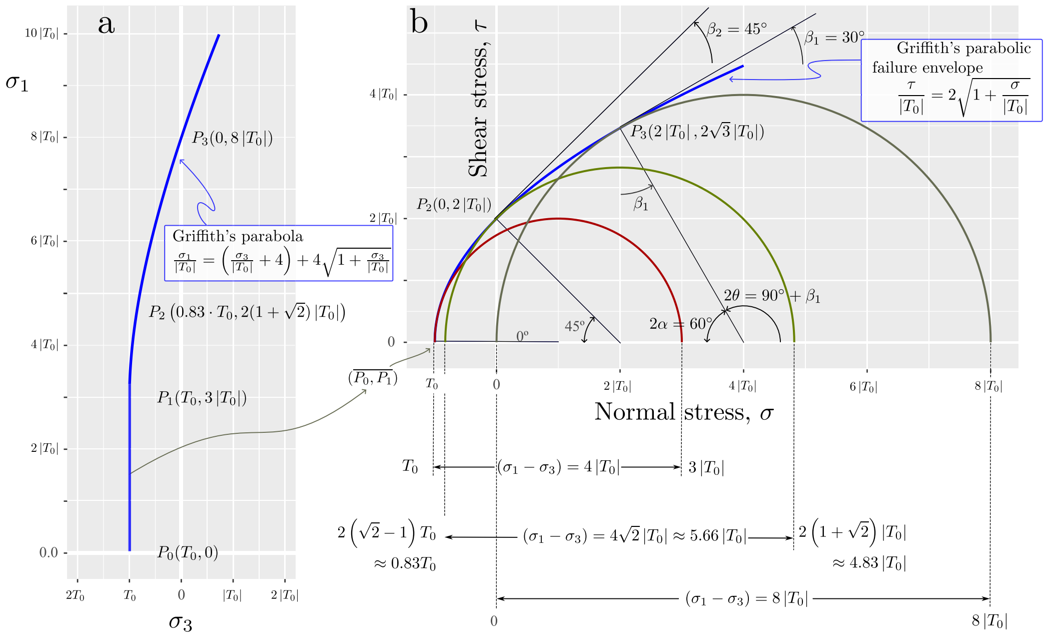

	σ_3	σ_1	σ	τ	β
P_0	T_0	0	T_0	0	90°
P_1	T_0	$3 \cdot \|T_0\|$	T_0	0	90°
P_2	$2(\sqrt{2}-1)T_0$	$2(1+\sqrt{2})\,\|T_0\|$	0	$2 \cdot \|T_0\|$	45°
P_3	0	$8 \cdot \|T_0\|$	$2 \cdot \|T_0\|$	$2 \cdot \sqrt{3} \cdot \|T_0\|$	30°

Fig. 2. Graphical expression of the OGC. (a) OGC failure parabola in the (σ_3, σ_1) space, expressed by scaling with the tensile strength, $|T_0|$. Pairs (σ_1, σ_3) that fall on the segment $\overline{(P_0, P_1)}$ will produce pure tensional fractures, orthogonal to σ_3. Pairs (σ_1, σ_3) touching the curve between P_1 and P_2 will produce oblique extension fractures formed under a negative normal stress σ. The curve segment P_2 to P_3 marks the formation of fractures under positive normal stress, albeit the minimum main stress, σ_3, is still negative. From P_3 onwards, is the dominion of shear fractures on compression, under positive main stresses. (b) OGC failure envelope in the (σ, τ) space. The pairs (σ_1, σ_3) are now circles, that when in contact with the failure parabola indicate fracturing of the rock. Three of such circles are represented in detail, with their respective values of σ, τ_α and the diameter of the circle $(\sigma_1 - \sigma_3)$. From left to right, the first circle represents the stress state with maximum σ_1 (that equals $3|T_0|$) that still yields pure tensile fractures. The second one corresponds to the stress state for which $\sigma = 0$. The third circle corresponds to the uniaxial compressive test ($\sigma_3 = 0, \sigma_1 = C_0$), and is the smallest stress differential that generates shear fractures fully in compression. (c) Coordinates of relevant points both in (σ, τ) space and in (σ_3, σ_1) space.

Table 1
Summary of the main equations of the Original Griffith Criterion (OGC) under various boundary conditions: when the normal stress is zero (transition to compressive failure conditions), under pure tensile loading (σ_3 equal to the tensile strength, T_0), and when $\sigma_3 = 0$, corresponding to uniaxial compression test conditions (σ_1 takes the value C_0 or σ_c, depending on the notation adopted). See Supplementary materials, section A for further details.

	$\sigma = 0$	$\sigma_3 = T_0$	$\sigma_3 = 0$
σ_1	$(2 + 2\sqrt{2})\,\|T_o\|$	$3\,\|T_o\|$	$8\,\|T_o\|$
σ_3	$(2 - 2\sqrt{2})\,\|T_o\|$	T_0	0
σ	0	T_0	$2\,\|T_o\|$
τ	$2\,\|T_o\|$	0	$2\,\|T_o\|\,\sqrt{3}$
β	45°	90°	30°
	$\frac{\tau}{\|T_0\|} = 2\sqrt{\left(\frac{\sigma}{\|T_0\|} + 1\right)}$	$\frac{\sigma}{\|T_0\|} = \frac{\sigma_3}{\|T_0\|} + 2\sqrt{1 + \frac{\sigma_3}{\|T_0\|}}$	$\frac{\sigma_1}{\|T_0\|} = \left(\frac{\sigma_3}{\|T_0\|} + 4\right) + 4\sqrt{1 + \frac{\sigma_3}{\|T_0\|}}$

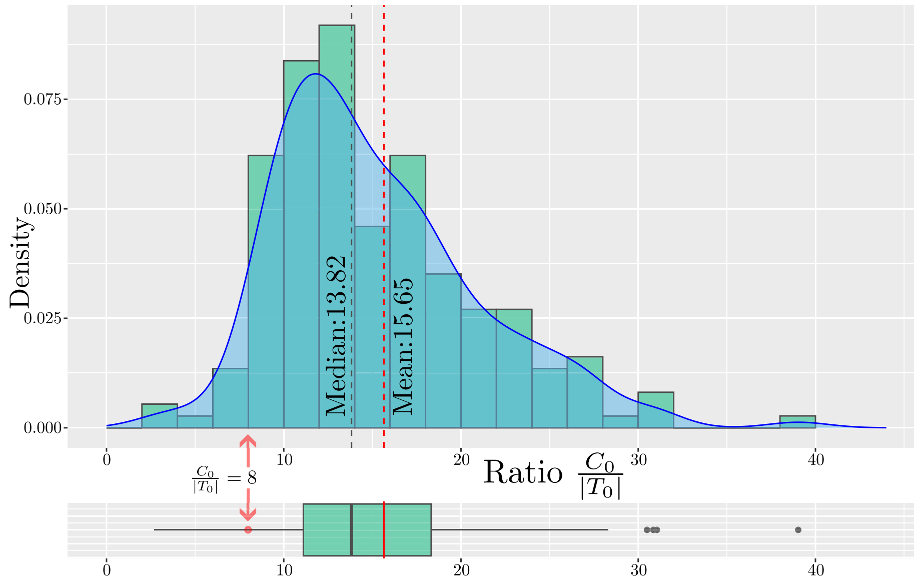

Fig. 3. Histogram, kernel density estimate, and boxplot of the C_0/T_0 ratio from 186 datasets derived from triaxial testing (Johnston, 1985; Cordón et al., 2024) and RocData™ v4.2. Vertical dashed lines indicate the mean (15.65) and median (13.82) of the distribution. The mark in the left whisker of the boxplot highlights the reference ratio $C_0/|T_0| = 8$, which lies below the first quartile and is therefore exceeded by more than 75% of the observations.

By combining this mathematical framework with fundamental concepts related to curved contact mechanics, it is possible to construct the envelope of a family of Mohr circles. This procedure yields parametric expressions for the normal stress $\sigma = \psi(\beta)$ and the shear strength $\tau = \eta(\beta)$ acting on the failure plane.

Both quantities are therefore defined parametrically in terms of the angle β, which represents the inclination of the tangent to the failure envelope with respect to the horizontal. This angle, also referred to as the instantaneous internal friction angle φ_i, is a function of the level of normal stress, and is governed by the following expression:

$$\left(\frac{\sigma}{C_0} - \xi\right) = (1-\sin\beta)\left\{ k_4 + \left(\frac{k_2}{2(1+k_1)}\right)^2 \frac{4k_1 + (3-k_1)\left[(1-k_1)+(1+k_1)\sin\beta\right]}{\left[(1-k_1)+(1+k_1)\sin\beta\right]^2} \right\} \tag{13}$$

The constant k_4, for intact rock, arises as an integration constant whose value must be determined according to the relevant boundary conditions. Through the application of regression techniques, the constant takes the following value:

$$k_4 = -\left[\frac{1}{8}\left(\frac{C_O}{|T_O|}\right) + \frac{1}{10}\right], \; R^2 = 1 \tag{14}$$

On the other hand, the analytical computation of the envelope—or intrinsic strength curve—is based on the assumption that the magnitude of the normal stress σ is known. Subsequently, the angle β is determined by applying an iterative technique that satisfies the condition $f(\sigma,\beta) = 0$. If the value of β is known, the normal stress can also be determined directly. Once both β and σ are available, the corresponding shear strength τ is computed using the following expression:

$$\left(\frac{\tau}{C_0}\right) = \left(\frac{\sigma}{C_0} - \xi\right)\cdot\tan\left(45^\circ + \frac{\beta}{2}\right) - \frac{\left(\frac{k_2}{2}\right)^2\cdot\tan\left(45^\circ+\frac{\beta}{2}\right)}{\left[\tan^2\left(45^\circ+\frac{\beta}{2}\right) - k_1\right]^2} \tag{15}$$

This formulation links the shear strength on the fracture plane to the corresponding normal stress and angle β, while incorporating correction terms that account for the microstructural and geometric characteristics of the failure process.

The constants k_1 and k_2 were obtained through the geometric properties of the parabola in analytical geometry by applying the concept of the *latus rectum*—the chord of a conic section that passes through the focus, is perpendicular to the major axis, and whose endpoints lie on the curve (Úcar, 2021).

$$k_1 = \frac{-(1+|\xi|) + \sqrt{(1+7|\xi|)(1-|\xi|)}}{2|\xi|} \tag{16}$$

and

$$k_2 = \frac{1 - k_1(-\xi)}{\sqrt{-\xi}} \tag{17}$$

This criterion has been thoroughly validated against experimental data (Cordón et al., 2024), with excellent results in both prediction mode (using only T_0 and C_0 as input data) and fitting mode (adjusting the criterion parameters to achieve the best fit to a set of triaxial test data). For a more mathematically robust fitting procedure, the orthogonal non-linear regression method described by Úcar et al. (2024) may be used.

4. A new formulation for the Griffith criterion (NGC)

After presenting the two theoretical pillars previously formulated and published (OGC and UC), and in view of the limitations of the former, we will now propose the changes that, in our opinion, could help improve it. In this section, we describe the modifications to the OGC, transforming Eq. (10) (see the details of its definition in the Supplementary Materials, section B: “Analytical procedure to define NGC”) to

$$\sigma_3 = T_0\text{, a vertical line, when: } \sigma_1 \le -\lambda\cdot T_0 \tag{18}$$

The second equation can also be expressed by considering the following plane curve:

$$\sigma_1 = C_0\cdot a\cdot\left(\frac{\sigma_3}{C_0} - \xi\right)^{3/4} + \lambda\cdot|T_0|\text{, when } \sigma_1 \ge -\lambda\cdot T_0 \tag{19}$$

Table 2
Summary of the boundary conditions and resulting equations used to determine the required parameters: a, λ, β_1, β_2, and $(\bar{\sigma}_3)_{\sigma=0}$. Full mathematical derivation and additional details are provided in Section B of the Supplementary Materials.

Boundary condition	Resulting equation
$\bar{\sigma}_3 = 0$, $\bar{\sigma}_1 = \frac{\sigma_1}{C_0} = 1$	$1 - a(-\xi)^{3/4} - \lambda\|\xi\| = 0$
$\bar{\sigma}_3 = 0,\ \beta = \beta_1$	$\sqrt{\frac{3a}{4}\frac{1}{(-\xi)^{1/4}}} - \tan\left(45° + \frac{\beta_1}{2}\right) = 0$
$(\bar{\sigma}_3)_{\sigma=0},\ \beta = \beta_2$	$3a\bar{\sigma}_3 + 4a\left(\bar{\sigma}_3 - \xi\right) + 4\left(\bar{\sigma}_3 - \xi\right)^{1/4} \cdot \lambda\|\xi\| = 0$
$(\bar{\sigma}_3)_{\sigma=0},\ \beta = \beta_2$	$\sqrt{\frac{3a}{4}\frac{1}{(\bar{\sigma}_3-\xi)^{1/4}}} - \tan\left(45° + \frac{\beta_2}{2}\right) = 0$
$\beta_1,\ \beta_2,\ I = f(\beta)$	$\xi + \left(1 - \sin\beta_2\right)\left[\left(\Omega_1\right)_{\beta=\beta_1} - 7\left(\frac{3a}{4}\right)^4 (I)_{\beta=\beta_2}\right] = 0$

From Eq. (19), the pure traction state is defined for $\sigma_3 = T_0$ and is therefore equivalent to writing $\sigma_1 \le \lambda|T_0|$. Consequently, hybrid fractures, variously referred to as hybrid, oblique extension fractures, bimodal, transitional-tensile, partial-opening, mixed-mode (Hancock, 1985; Suppe, 1985; Price and Cosgrove, 1990; Bahat, 1991; van der Pluijm and Marshak, 2004; Twiss and Moores, 2007; Davis et al., 2011; Reeher et al., 2023), are often defined in the interval $T_0 \le \sigma_3 \le 0$.

The parameters for the NGC, λ and a, are obtained from the analysis of boundary conditions by solving a system of non-linear equations (see Supplementary Materials, section B: "Analytical development"), though an alternative procedure is presented shortly.

It is also noteworthy that the ratio $C_0/|T_0| = 1/|\xi|$ plays a key role in the values of the aforementioned constants, and consequently in the magnitude of the stress field acting upon the rock mass.

Table 2 shows the equations derived from the boundary conditions; their obtention is detailed in section B of the Supplementary Materials.

By solving the system of equations presented in Table 2, the values of the parameters a and λ were obtained for each dataset included in Fig. 3, using an R script (available in the Supplementary Materials).

Fig. 4 displays the relationships between these parameters and the value of ξ (more precisely, with its absolute reciprocal, $1/|\xi|$). As shown, the correlations are of sufficiently high quality to allow, if desired, the omission of the optimisation procedure in R or in a spreadsheet, and instead simply apply the empirical correlation expressions:

$$a = 0.531 \cdot \left(\frac{1}{|\xi|}\right)^{0.75} = 0.531 \cdot \left(\frac{C_0}{|T_0|}\right)^{3/4} \tag{20}$$

correlation with a R^2 value of 0.99985, and

$$\lambda = 0.472 \cdot \left(\frac{1}{|\xi|}\right) = 0.472 \cdot \left(\frac{C_0}{|T_0|}\right) \tag{21}$$

with a R^2 virtually equal to 1.

Table 3 shows the results obtained using the different approaches to determine the relevant parameters for a specific case: a rock with $C_0 = 25$ MPa, $T_0 = -2.5$ MPa and therefore, $\xi = -0.1$ and $C_0/|T_0| = 10$. The equations of the analytical approach are implemented in the R script of the Supplementary Materials. The equations obtained in this section for the alternative procedure were implemented using a handheld calculator.

Once a robust formulation for the NGC has been established in the (σ_3, σ_1) space, it is pertinent to derive the formulation for the envelope in the (σ, τ) space.

$$\frac{\sigma}{|T_0|} = \frac{1}{2}\left[\left(\frac{\sigma_1}{|T_0|} + \frac{\sigma_3}{|T_0|}\right) - \sin\beta\left(\frac{\sigma_1}{|T_0|} - \frac{\sigma_3}{|T_0|}\right)\right] \tag{22}$$

and

$$\frac{\tau}{|T_0|} = \frac{1}{2}\left(\frac{\sigma_1}{|T_0|} - \frac{\sigma_3}{|T_0|}\right)\cos\beta \tag{23}$$

where $\overline{\sigma_1} = a\left(\overline{\sigma_3} - \xi\right)^{3/4} + \lambda\,|\xi|$, $\overline{\sigma_1} = \frac{\sigma_1}{C_0}$, and $\overline{\sigma_3} = \frac{\sigma_3}{C_0}$

Table 3
Values obtained with the two procedures included in this work (with the abacus we can obtain the values of a and λ and, from that point, the rest of parameters either via the rigorous or the alternative method).

	Rigorous	Alternative
a	2.97	2.99
λ	4.72	4.72
β_1	47.6°	47.6°
β_2	36.6°	36.7°
$\sigma_{1_{\sigma=0}}$ (MPa)	14.58	14.45
$\sigma_{3_{\sigma=0}}$ (MPa)	−2.19	−2.19

Table 4
Values of the envelope slope at the ordinate intercept ($\beta_{(\sigma=0)}$) and at uniaxial compressive failure ($\beta_{(\sigma_3=0)}$), and of the shear strength at zero normal stress ($\tau_{(\sigma=0)}$), for $C_0/|T_0|$ ratios between 4 and 12 for the NGC, together with the corresponding values obtained using the OGC.

Ratio $C_0/\|T_0\|$	$\beta_{(\sigma=0)}$	$\beta_{(\sigma_3=0)}$	$\tau_{(\sigma=0)}$
4	26.9°	13.2°	$1.43\|T_0\|$
6	36.8°	24.2°	$1.75\|T_0\|$
8	43.1°	31.5°	$2.02\|T_0\|$
8 (OGC)	45°	30°	$2.00\|T_0\|$
10	47.6°	36.4°	$2.26\|T_0\|$
12	51.0°	40.6°	$2.47\|T_0\|$
14	53.7°	44.1°	$2.67\|T_0\|$

NGC parameters, a and λ, can be obtained from Eqs. (20) and (21). For the particular case where $\sigma = 0$:

$$\left(\sigma_3\right)_{\sigma=0} = \left(\frac{7}{8}\right) T_0 \tag{24}$$

Similarly, τ when $\sigma = 0$ (intercept at origin):

$$\tau_{(\sigma=0)} = \frac{5}{7} \cdot |T_0| \cdot \sqrt{\frac{C_0}{|T_0|}} \tag{25}$$

Finally, as Eqs. (22) and (23) express σ and τ as functions of β, we need the value of this angle (in the Supplementary Materials, where the underlying mathematical derivations are presented, we derive equations relating key parameters — including the failure envelope slope β at each point and the pairs of failure stresses (τ, σ_n) — to the $C_0/|T_0|$ ratio):

$$\beta = 2\theta - 90° = 2 \cdot \arctan\left(\sqrt{\frac{3a}{4\left(\bar{\sigma}_3 - \xi\right)^{1/4}}}\right) - 90° \tag{26}$$

Thus, for the NGC, these relationships can be quantified across the range of ratios most prevalent in experimental datasets (approximately 4 to 30). Recall that the OGC model features several key parameters that remain constant (see Table 1), including a fixed $C_0/|T_0|$ ratio of 8. Applying Eqs. (22), (23), and (26), the corresponding NGC values (Table 4) can thus be derived for several ratios, including $C_0/|T_0| = 8$, and directly compared with those of the OGC.

The comparison presented in Table 4 demonstrates that, for all practical purposes, the OGC constitutes a specific case of NGC when $C_0/|T_0| = 8$. This, in turn, suggests that the NGC represents a natural extension of the OGC, whereby the fixed ratio $C_0/|T_0| = 8$ is abandoned in favour of variable ratios supported by experimental evidence (see Fig. 3).

5. The challenge of combining the NGC and UC curves

The formulation of the failure criteria developed in the previous sections (UC and NGC) allows us to face the central challenge of this

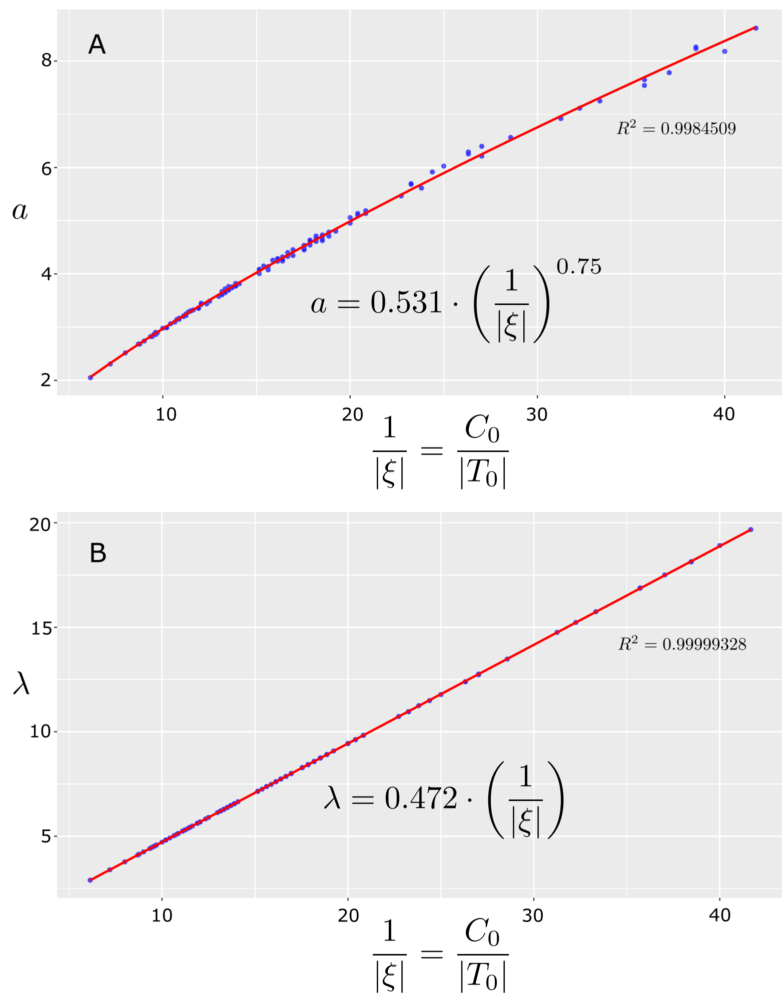

Fig. 4. Correlations derived from the eqs. in Table 2, based on the solutions to the NGC formulation applied to the considered dataset. (a) Relationship between the parameter a and the inverse of $|\xi|$, with the fitted power-law expression and its corresponding coefficient of determination ($R^2 = 0.9985$) shown in the graph. (b) Correlation between λ and $1/|\xi|$, exhibiting a near-perfect linear fit ($R^2 = 0.99999$). The strong correlations suggest that these expressions may serve as practical approximations, potentially replacing the need for direct equation solving in applied contexts.

work: finding the most accurate connection between the compressive and extensional failure curves. We should remember that this challenge has been addressed by many authors over decades (see section 1.2) and that such a connection has been located at various points in the (σ, τ) space, always within segment 3 of Fig. 1: either at its left end (point P2 in Fig. 2, adopted by the "Modified Griffith Criterion": Brace, 1960; McClintock and Walsh, 1962), its right end (point P3 in Fig. 2, implicitly assumed by Hancock, 1985), or its centre (Sibson, 1998).

In our case, the criterion selected to define the transition between the two failure models is the point at which the system fully enters a compressive regime—namely, when the minimum effective principal stress, σ_3, becomes positive. Accordingly, the NGC is considered valid within the range from T_0 up to $\sigma_3 = 0$, whereas the UC criterion applies from $\sigma_3 = 0$ onwards, as long as the rock maintains brittle behaviour.

It is therefore desirable for both criteria to converge at $\sigma_3 = 0$. That is, if considered in the (σ, τ) space, both should predict identical values of τ, σ, and β_2 at $\sigma_3 = 0$. As shown in Fig. 5, although the transition between the two curves is acceptably smooth, a slight overlap can be observed, while the tangent angle does not match exactly. Similarly, in the (σ_3, σ_1) space, although both curves do join at $\sigma_3 = 0$, they do so with a slightly different tangential slope.

These discrepancies are, of course, a direct consequence of the fact that the UC and NGC equations were derived independently. It has been verified that minor adjustments to the main input parameters (C_0, T_0, within their experimental error bars, and fine-tuning of a and λ via a fitting function) can reduce the differences in both values and angles to a negligible level. However, we have chosen to preserve the original parameter values, and the derived quantities, in order to maintain internal consistency.

Fig. 6 shows the composite NGC+UC failure criterion for the most common range of $C_0/|T_0|$ ratios (see Fig. 3), using dimensionless axes normalised with respect to the tensile strength $|T_0|$. Normalisation with respect to $|T_0|$ enables a direct comparison of how the ratio $C_0/|T_0|$ influences the shape and extent of the composite failure envelope. Each one represents the failure curve corresponding to a specific value of this ratio. The red curve corresponds to the particular case defined by the NGC criterion, where $C_0/|T_0| = 8$.

In Fig. 6A, the variation of the combined failure criterion is shown in the (σ_3, σ_1) space for several values of the ratio $C_0/|T_0|$. Fig. 6B displays the corresponding curves in the (σ, τ) space, i.e., Mohr coordinates, for the same set of ratios. The envelopes are colour-coded consistently: blue for NGC, orange for UC, and red for OGC. All curves were generated

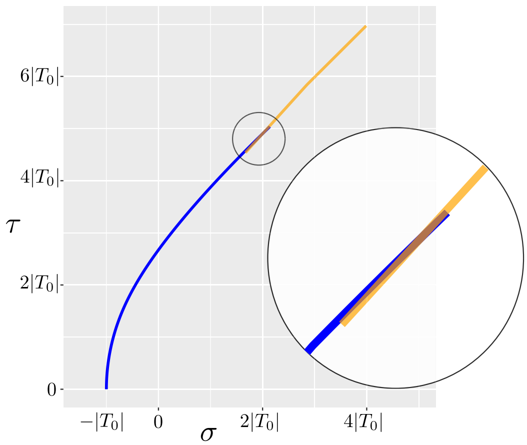

Fig. 5. Generic dimensionless case represented in the (σ, τ) space, assuming $T_0 = -1$ and $C_0 = 10$. The transition region between the new Griffith Criterion (NGC, blue) and Úcar's Criterion (UC, orange) is magnified on the right. Despite both curves being generated with the same values of C_0 and T_0, their independent formulations lead to slight differences in the predicted values of $(\sigma)_{\sigma_3=0}$ and in the angle β_2, resulting in a small, slightly rotated overlap between both envelopes.

using the corresponding ratio parameter values for λ, a, and $\xi = T_0/C_0$. The connection between both curves in the (σ, τ) space is quite accurate for any value of the strength ratio $C_0/|T_0|$. Despite the difference in coordinates between their ends, the overlap between curves is well within typical experimental uncertainty. It is also interesting to highlight the improvement in this connection compared to that provided by the OGC formulated for the particular case of the ratio $C_0/|T_0| = 8$. It can be observed in both panels that the OGC curve ($C_0/|T_0| = 8$) lies significantly below the UC curve for segment 4 of Fig. 1, that is, for stress states to the right of Point P3 of Fig. 2. This is consistent with the previously mentioned behaviour of the OGC criterion, which tends to underestimate rock strength under compressive regimes—i.e., when both σ_1 and σ_3 are positive, whereas Úcar's curve usually fits the experimental data very well (Cordón et al., 2024; Úcar et al., 2024).

5.1. Experimental validation of the combined criterion

Figs. 7 and 8 illustrate selected examples of triaxial test data plotted against the predicted failure envelopes obtained from the new Griffith Criterion (NGC) and Úcar's Criterion (UC), using the corresponding values of uniaxial compressive strength (C_0) and tensile strength (T_0). The datasets include conventional uniaxial and triaxial compression tests, as well as confined extension tests.

Panels a and b of Fig. 7 show the behaviour of Carrara marble as reported by McCormick and Rutter (2022), while panels c and d present data for Berea sandstone from Bobich (2005). In both cases, the NGC and UC envelopes capture the overall failure trend in the (σ_3, σ_1) and Mohr stress spaces. The zoomed view in panel a reveals the transition between compressive and extensional regimes, where the slight divergence between the two models becomes more evident. Panels e and f of Fig. 8 present additional triaxial data for Carrara marble from Ramsey and Chester (2004), and panels g and h show results for Dunnville sandstone from Tarokh et al. (2022). Ramsey and Chester (2004) classified their experimental results according to the character of the fractures produced. The NGC successfully identifies the transition from purely tensile to hybrid fractures, placing it between the tensile fracture associated with higher σ_1 values and the hybrid fracture occurring at lower σ_1.

These cases illustrate that the combined NGC and UC curves — recall that they are obtained by simply inputting the values of T_0 and C_0 into the corresponding equations — show remarkably good agreement with the experimental data across a wide range of failure stress conditions. As such, they can be considered effective predictors of the failure behaviour of the corresponding rocks, both in extension and in compression.

5.2. Examples of application

Inspired by the classical examples of Suppe (1985) and Gudmundsson (2011), we may consider a couple of application cases — well suited for classroom exercises — that illustrate the potential usefulness of having a mathematical and numerical formulation of the combined failure criterion.

Example 1

A given sedimentary rock is affected by both purely extensional joints and hybrid shear fractures. Assuming that the entire sequence was saturated at the time of fracturing, and given the following values:

- Poisson coefficient $\nu = 0.22$
- Biot coefficient $\alpha = 1$
- Unit weight $\gamma = 25.5$ kN/m^3
- Strength parameters: $C_0 = 25$ MPa, $T_0 = -2.5$ MPa
- Tectonic horizontal extensional regional field estimated to be -5 MPa

At what depths could the different types of structures have formed?

General framework. Using Fig. 2a as a reference: Pure extensional fractures will occur when the pair σ_3, σ_1 lies along the vertical segment $P_0 - P_1$, which, in the NGC criterion, corresponds to $\sigma_3 = T_0$ and $\sigma_1 \leq -\lambda T_0$. Transitional or hybrid shear fractures are expected to occur from point P_1 up to P_3, that is, as long as $\sigma_1 \leq C_0$, provided that σ_3 remains below the threshold defined by the failure criterion.

Development. Given that $C_0 = 25$ MPa and $T_0 = -2.5$ MPa, then $\xi = 10$. We can compute the relevant parameters for the NGC criterion as follows:

$$\lambda = 0.472 \cdot 10 = 4.72 \quad \text{and} \quad a = 0.531 \cdot 10^{0.75} = 2.986$$

With the values of C_0, T_0, ξ, a, and λ determined, the NGC and UC curves — and their corresponding value tables — can now be generated for this rock. This will allow a direct comparison between the stress thresholds for fracture generation and those predicted by the combined criterion.

The thresholds for the example considered are therefore:

- Tensile fractures, $\sigma_1 < 4.71 \cdot 2.5 = 11.7$ MPa. $\sigma_3 \leq T_0$
- Hybrid fractures, $11.7 < \sigma_1 < 25$ MPa, $\sigma_3 \leq \sigma_{3NGC} \leq 0$
- Shear fractures, 25 MPa $< \sigma_1$, $0 \leq \sigma_3 < \sigma_{3UC}$

We may now consider possible combinations of depth within the stratigraphic sequence and tectonic stress values that satisfy the above conditions. Let us denote the tectonic stress by TS, which will be negative under extensional regimes. The stress state at a given depth can then be calculated as follows:

$$\left.\begin{aligned} P_f &= \gamma_w \cdot z \\ \sigma_1 &= \gamma \cdot z \\ \sigma_1 &= \sigma_1 - \alpha \cdot P_f \\ \sigma_3 &= \frac{\nu}{1-\nu} \cdot \sigma_1 + TS \end{aligned}\right\}$$

It is therefore sufficient to assign values to z for each considered instance of TS, which in this case is set to -5 MPa, and compare the resulting stress states with the previously defined conditions. The results are summarised in Table 5.

Given that the tensile strength is $T_0 = -2.5$ MPa, purely extensional fractures may form from the surface down to a depth of approximately 630 m. Beyond this point, the differential stress becomes too large

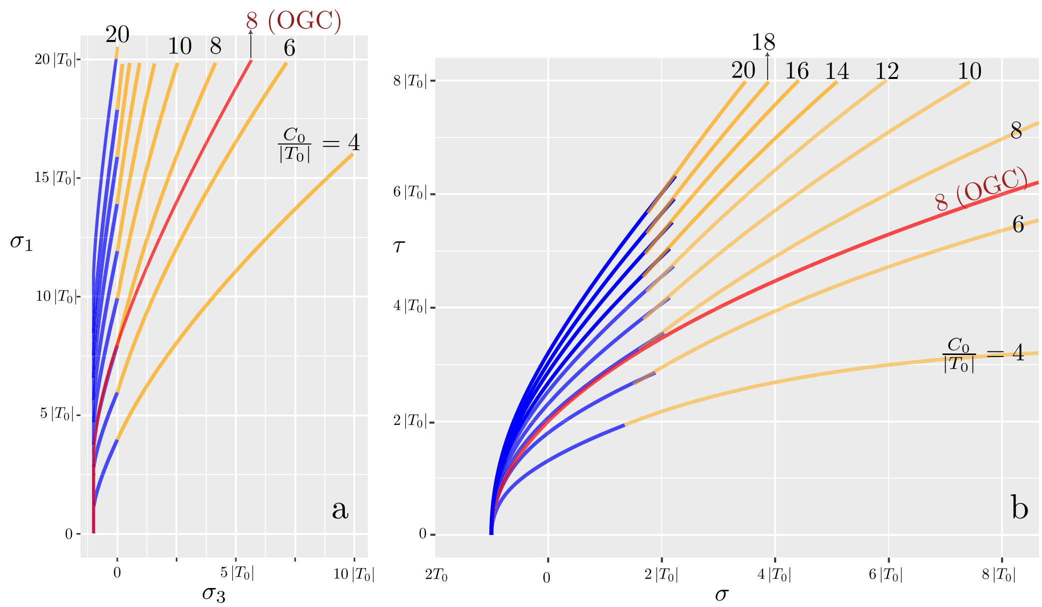

Fig. 6. Combined failure envelopes based on the new Griffith Criterion (NGC, in blue) for the tensile regime and the Úcar Criterion (UC, orange) for the compressive domain, represented for various values of the strength ratio $C_0/|T_0|$. (a) Failure envelopes in the principal stress space (σ_3, σ_1), normalised with respect to the tensile strength $|T_0|$. (b) Corresponding envelopes in the Mohr space (σ, τ), also normalised by $|T_0|$ for different ratios of $C_0/|T_0|$. Curves are shown for a range of strength ratios from 4 to 20. The red curve, in both panels, corresponds to the case $C_0/|T_0| = 8$, that is to say, the OGC.

Table 5
Results of a model with $TS = -5$ MPa. See text for further details.

Type of fracture	Min. depth	Max. depth
Tensile	0 m	633 m
Hybrid shear	633 m	1786 m

to allow their formation, and they are progressively replaced by hybrid fractures. These, in turn, become mechanically unfeasible below approximately 1790 m.

It should be noted that this analysis does not account for the possible occurrence of overpressure within specific stratigraphic levels, which could facilitate the formation of what would technically be classified as hydrofractures. Additionally, the model assumes a homogeneous lithological sequence; incorporating heterogeneity would necessarily increase the complexity of the stress–depth relationship due to variable effective stress gradients.

Example 2

Consider a hypothetical rock mass located at a depth of 5 km and at a temperature of 450 K. Its geothermal potential is assumed to be exploited by means of a cooling process intended to enhance reservoir productivity. The objective is to determine the temperature drop between the injection and extraction boreholes required to induce thermal fracturing in the rock mass. The numerical values adopted in this example are purely illustrative and are intended only to demonstrate the proposed analytical procedure.

- Elastic modulus E = 40 GPa,
- Poisson coefficient v = 0.25
- Biot coefficient $\alpha = 1$
- Average unit weight $\gamma \approx 25 \mathrm{kN/m^3}$
- Linear thermal expansion coefficient $\alpha_t = 1.0 \times 10^{-5}\ \mathrm{K^{-1}}$
- Strength parameters: $C_0 = 25$ MPa, $T_0 = -2.5$ MPa.

Conceptual framework: In a confined, isotropic medium, thermal cooling induces volumetric contraction, which is mechanically resisted by the surrounding confinement. As a result, this contraction generates additional stresses in all confined directions. In a fully confined three-dimensional element, a temperature decrease thus induces compressive (or tensile, in the case of cooling) stresses along all three principal directions.

Therefore, under the assumption of isotropy and full confinement — reasonable at a depth of 5 km — the thermal stress increment will affect both σ_V and σ_H equally.

The formulation begins with an initial stress state defined by the effective vertical and horizontal stresses at 5 km depth prior to cooling. These are given by:

$$\sigma_V = \gamma' \cdot z \quad \text{and} \quad \sigma_H = k_0 \cdot \sigma_V$$

Subsequently, following the cooling process, the stress state is modified by a thermal term that introduces an additional stress component. Assuming the medium remains confined and isotropic, the thermally induced stress increment is uniform and can be expressed as:

$$\Delta T_0 = \frac{\alpha_t \cdot E}{1 - \nu} \cdot \Delta T$$

This thermal term is added (subtracted, in the present case) to each of the principal effective stresses, resulting in a new stress state:

$$\sigma_{V\,final} = \sigma_V - \Delta T_0$$
$$\sigma_{H\,final} = k_0 \cdot \sigma_{V\,final} - \Delta T_0$$

Thus, the cooling process effectively shifts the entire stress field towards tension. If the thermal stress increment is sufficiently large, it may cause the modified stress state to intersect the failure envelope, thereby inducing thermal fracturing.

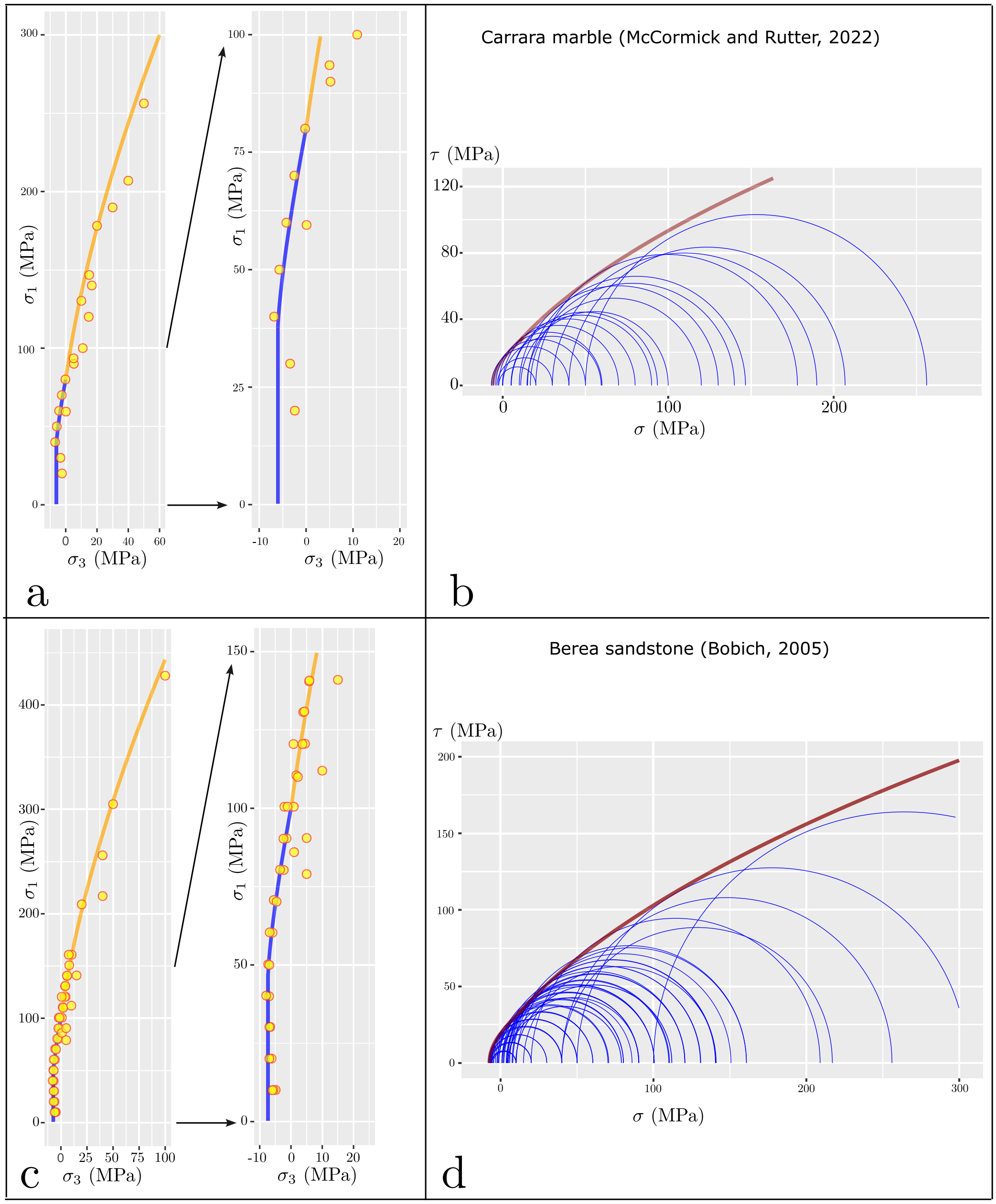

Fig. 7. Examples of triaxial data, including confined extension tests, plotted alongside the predicted failure envelopes based on NGC and UC, using values of C_0 and T_0 as input. (a) Triaxial tests on Carrara marble (yellow circles), from McCormick and Rutter (2022), plotted in (σ_3, σ_1) space. The dataset includes both conventional and confined extension tests. The NGC envelope is shown in blue; UC in orange. Left: full data range; right: zoom into the transition region. (b) Same dataset as in (a), represented in Mohr space. (c) Triaxial data for Berea sandstone from Bobich (2005), also plotted in (σ_3, σ_1) space with the same colour scheme. (d) Mohr space representation of the dataset in C. For clarity, the Mohr circles corresponding to the two tests at highest confining stress have been truncated.

This formulation is valid under the following key assumptions: the medium is considered linearly elastic and isotropic, the thermal strain is applied uniformly throughout the volume, and the rock is fully confined.

However, if the cooling is non-isotropic — for instance, due to cold fluid injection generating radial temperature gradients — then the variation in thermal stress primarily affects the tangential (i.e., horizontal) directions, while the vertical stress remains governed by overburden weight and is largely unaffected.

Such a scenario may more accurately represent a radial geothermal stimulation process, in which cold fluid injection induces circumferential fracturing by generating thermal tension in the horizontal plane.

Development: In R, we simulate temperature drops within a predefined range (initially 0 to −30 K, in increments of 0.1 K) for a rock mass located at a depth of 5000 m. For each cooling step, we calculate the resulting effective vertical and horizontal stresses, σ_v and σ_h, and compare them to the failure envelope defined by a combined NGC+UC

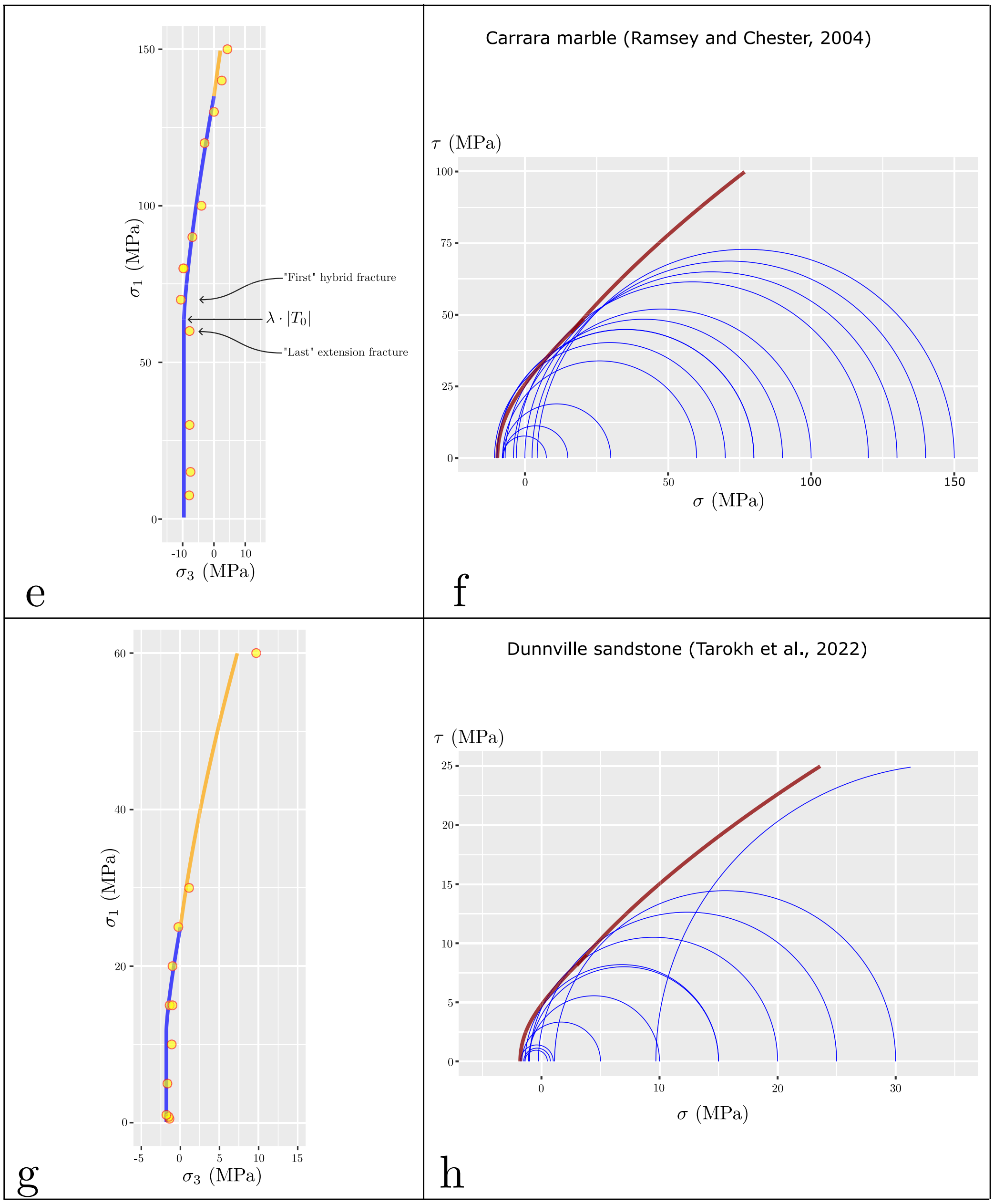

Fig. 8. Additional examples of triaxial data plotted against predicted failure envelopes based on the NGC (blue) and UC (orange), using the corresponding values of C_0 and T_0. (e) Triaxial tests on Carrara marble (yellow circles) from Ramsey and Chester (2004), represented in (σ_3, σ_1) space. The arrow *"Last" extension fracture* identifies the experimental pair (σ_2, σ_1) with higher value of σ_1 that the mentioned authors considered to produce an extensional fracture. Similarly with the *"First" hybrid fracture*. Arrow $\lambda \cdot |T_0|$ identifies the transition point between tensile and hybrid fractures for this data set according to NGC. (f) Same dataset as in E, shown in Mohr space. (g) Triaxial data for Dunnville sandstone from Tarokh et al. (2022), plotted in (σ_3, σ_1) space. (h) Mohr space representation of the dataset in G. For clarity, the Mohr circle corresponding to the test at highest confining stress has been truncated.

curve provided in CSV format. This envelope was previously computed based on the rock strength parameters used in this case.

Specifically, at each temperature step, we compute σ_1 and σ_3, and then interpolate the NGC+UC envelope to determine the minimum principal effective stress required to reach failure, given the current value of σ_3:

$$\sigma_{1\ \text{failure}} = f(\sigma_3)$$

Fracturing is predicted to occur when the following condition is met:

$$\sigma_1 \geq \sigma_{1\ \text{failure}\ \sigma_3} \quad \Rightarrow \quad \text{fracture}$$

The last five steps of the simulation (with ΔT increments of 0.1 K) are shown in the summary table, where the onset of failure is detected for a temperature drop of approximately $\Delta T \approx -18.9$ K.

In Fig. 9, to enhance graphical readability, the temperature step is displayed every 2 K, which improves visual clarity at the expense of resolution.

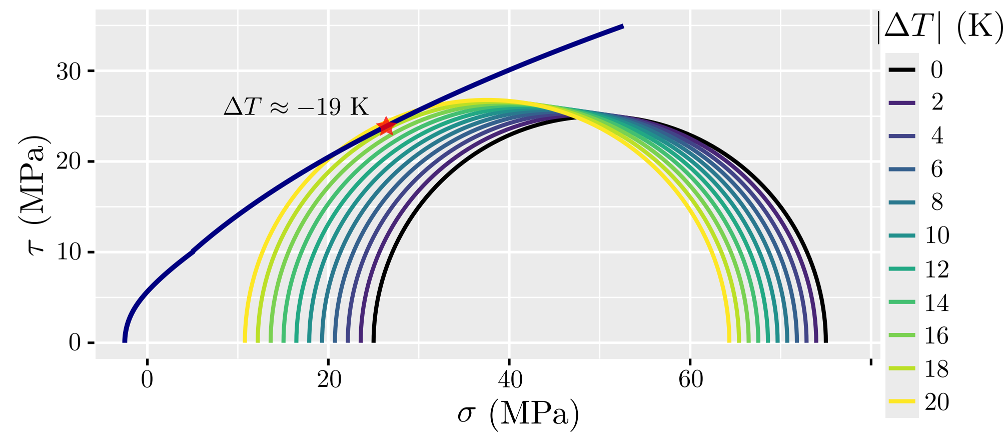

Fig. 9. Simplified representation of the procedure. Instead of the 0.1 K increments shown in Table 6, temperature steps of 2 K are displayed. The second-to-last circle corresponds to $\Delta T = -18$ K and does not yet reach the NGC+UC failure envelope. Failure would occur at approximately $\Delta T = -19$ K, but the last circle shown already exceeds the envelope. In this case, the script halted upon detecting the first circle that intersects the failure envelope; however, due to the 2 K step size, the critical $\Delta T = -19$ K value was skipped.

Table 6
Results of the numerical comparison, skipping to the last five tests.

ΔT (K)	σ_1 (MPa)	σ_3 (MPa)	σ_1 NGC+UC	Result
0	75	25	96.066	No fracture
…	…	…	…	…
18.5	65.133	11.844	65.603	No fracture
18.6	65.080	11.773	65.415	No fracture
18.7	65.026	11.702	65.228	No fracture
18.8	64.973	11.631	65.041	No fracture
18.9	64.920	11.560	64.853	Fracture

5.2.1. Example 3

The previous illustrative example is now extended into a parametric thermo-mechanical analysis:

Simulation framework. The simulation models the thermo-mechanical response of a rock mass located at a depth of $z = 5000$ m subjected to progressive cooling in order to determine the combinations of the thermal expansion coefficient (α) and temperature decrease (ΔT) that induce fracturing for a given value of Young's modulus.

Fixed input parameters (known values) include:

- Depth $z = 5000$ m.
- Average effective unit weight of the overburden $\gamma_{\text{eff}} = 15$ kN/m^3.
- Poisson's ratio $\nu = 0.25$.
- Biot's coefficient $\alpha = 1$
- Initial temperature $T_{\text{ini}} = 450$ K.
- Compressive ($C_0 = 25$ MPa) and tensile ($T_0 = -2.5$ MPa) strengths, along with the corresponding ratio $\xi = T_0/C_0$.

From these constants, additional model parameters are derived: the in-situ vertical stress $\sigma_{v,\text{ini}}$, the at-rest coefficient $k_0 = \nu/(1-\nu)$, and the coefficients of the Úcar criterion (k_1, k_2) and the new Griffith Criterion (NGC) (a, λ) based on empirical correlations with ξ.

Variables with defined ranges are:

- Thermal expansion coefficient $\alpha_t \in [0.8\times10^{-6},\ 1.5\times10^{-6}]$ K^{-1}.
- Young's modulus $E \in \{30, 40, 50, 60 \text{ GPa}\}$.
- Temperature decrease $\Delta T \in [0, 30]$ K.

Stress calculations:

For each combination of $\alpha_t, E, \Delta T$, the thermally induced stress change is calculated as: $\Delta\sigma_{th} = \dfrac{\alpha_t \cdot E}{1-\nu}\Delta T$. This increment is subtracted from the initial vertical stress to obtain the updated principal stresses: $\sigma_v = \sigma_{v,\text{ini}} - \Delta\sigma_{th}$, $\quad \sigma_h = k_0\,\sigma_v - \Delta\sigma_{th}$. The major and minor principal effective stresses are then assigned as: $\sigma_1 = \max(\sigma_v, \sigma_h)$, $\quad \sigma_3 = \min(\sigma_v, \sigma_h)$.

Fracture conditions:

Failure is assessed using a combined criterion:

1. Compressive regime ($\sigma_3 > 0$): The Úcar criterion (UC) is applied, with fracture occurring when for a given value of σ_3: $\sigma_1 \geq \sigma_{1,\text{UC}}$, where $\sigma_{1,\text{UC}}$ is the UC predicted value of σ_1 at failure for that σ_3.
2. Tensile regime ($\sigma_3 < 0$):
   - If $\sigma_1 \geq -\lambda \cdot T_0$, fracture is checked against the NGC expression: $\sigma_1 \geq C_0 \cdot a \cdot \left(\dfrac{\sigma_3}{C_0} - \xi\right)^{3/4} + \lambda \cdot |T_0|$.
   - If $\sigma_1 < -\lambda \cdot T_0$, fracture occurs when $\sigma_3 \leq T_0$.

Simulation output:

For each value of E, Young's modulus, the model identifies the minimum ΔT required to induce fracture for each α_t. These critical ($\alpha_t, \Delta T$) pairs define fracture boundary curves in the $\Delta T - -\alpha_t$ space. The output (this procedure is implemented in an R script available as Supplementary Material to this paper) includes:

- A full dataset of stress states and fracture classification ("fails" or "no fail").
- CSV export of all evaluated combinations.
- Graphical representation (Fig. 10) of the fracture boundaries for each E, enabling direct comparison of thermo-mechanical sensitivity across stiffness values.

6. Final remarks

Throughout this work, we have managed to formulate a combination of criteria (NGC and UC) that shows the continuity between rock failure processes under extensional and compressive conditions. The curves representing these criteria in the (σ, τ) space connect in a

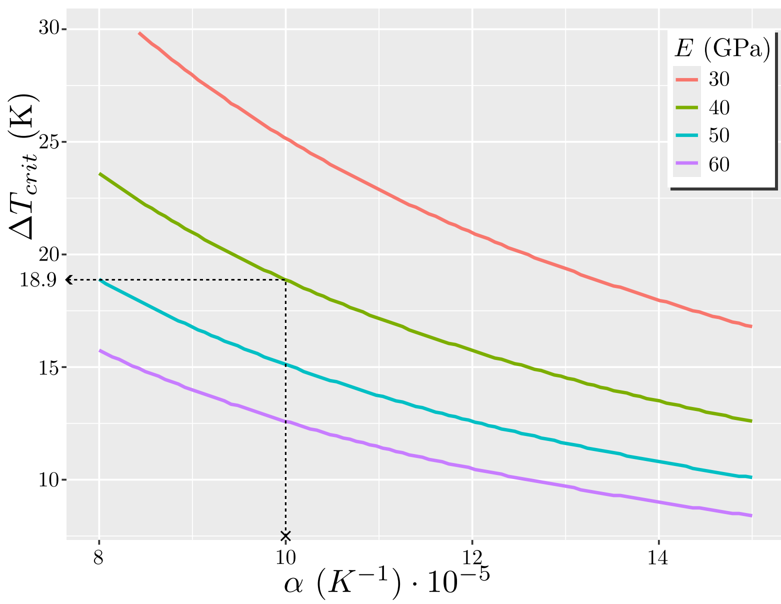

Fig. 10. Critical temperature drop $(\Delta T_{\mathrm{crit}})$ required to induce fracture as a function of the thermal expansion coefficient α for four values of Young's modulus E (30, 40, 50, and 60 GPa). The curves represent the fracture boundaries obtained from the combined new Griffith–Úcar criterion, considering the full range of parameter uncertainties defined in the simulation. The dotted lines illustrate the result of the Example 2, a simplified prior analysis, in which no variability ranges were assigned to the model parameters, yielding a single $(\alpha, \Delta T_{\mathrm{crit}})$ point for comparison.

very satisfactory manner, more than the proposals found in previous literature. This combination represents a coherent model that is entirely integrated into the existing theoretical framework. It does not attain the category of a "unified theory", but in practice, it constitutes a useful and consistent toolbox. It is encouraging to envisage that, in the not-too-distant future, new theoretical developments and new experimental tests will lead to the creation of a truly unified rock failure theory, represented by a single equation and a single envelope.

In the meantime, it is worth making some final considerations concerning the "meeting point" of the proposed curves and its confidence level.

Such a meeting point has been located at the boundary between the fully compressive stress mode ($\sigma_3 > 0$) and the mixed mode ($T_0 < \sigma_3 < 0$) (see Fig. 1). This was expected given our original reasoning: the NGC criterion is assumed within the range from T_0 to $\sigma_3 = 0$, while UC applies from $\sigma_3 = 0$ onwards. Both curves therefore converge at $\sigma_3 = 0$ in the (σ_3, σ_1) space.

The mechanical basis for setting such a boundary was established early by Griffith (1924): minor internal cracks in the rock body induce tensile stresses large enough for fracture propagation, even if the σ component is positive; Griffith's theory can therefore be considered valid at least as long as the minimum principal stress σ_3 is negative. The notion that, under compressive conditions, macroscopic shear fractures develop through the linkage of *en-échelon* interacting tensile cracks is well established in the literature (e.g., Brace and Bombolakis, 1963; Peng and Johnson, 1972; Segall and Pollard, 1983; Reches and Lockner, 1994; Engelder, 1999; Ramsey and Chester, 2004; McCormick and Rutter, 2022). It provides further support for the prevalence of Griffith's theory, regardless of whether it is formulated as the OGC or the NGC.

We have emphasised the fact that the connection between NGC and UC envelopes within the (σ, τ) space is quite precise; i.e., our combined failure criteria are functionally robust. Nevertheless, the slight misfit due to the fact that UC and NGC equations have been independently derived should be analysed in order to assess the resulting operational errors. We next inspect separately the dispersion or range that the overlap zone between curves represents in terms of stress values (σ and τ components) and slope, for ratios $C_0/|T_0|$ from 4 to 20. Errors in stress values mainly concern engineering geology and rock mechanics, while differences in the slope of the envelope (and hence in α angles between σ_1 and fractures) are of utmost interest to structural geology.

Concerning τ values, the distance between the tips of the respective curves (Range $\tau/|T_0|$) ranges from 0.03 for $C_0/|T_0| = 4$ to 0.66 for $C_0/|T_0| = 20$ (see Fig. 11b). Although those distances are appreciable, the difference in $\tau/|T_0|$ between both curves ($\Delta\tau/|T_0|$) is more significant. Adopting the intersection point between them as the optimum connection, the maximum error in $\Delta\tau$ ranges from 0.00 for $C_0/|T_0| = 4$ to 0.04 for $C_0/|T_0| = 20$ (Fig. 11d). In all cases, this error is symmetrically distributed with respect to the intersection point (compare $\Delta\tau R$ and $\Delta\tau L$ for each $C_0/|T_0|$ ratio).

Concerning $\sigma/|T_0|$ values (Fig. 11a), the distance between the curve tips (Range σ) starts from 0.026 to 0.49, and the resulting maximum error $\Delta\sigma$ ranges from 0.00, for $C_0/|T_0| = 4$, to 0.05, for $C_0/|T_0| = 6$ (Fig. 11c). In this case, the distribution is neither symmetric nor regular: the minimum $\Delta\sigma/|T_0|$ between NGC and UC envelopes at the overlap zone is 0 for $C_0/|T_0| = 4$ while it sharply increases up to the maximum for $C_0/|T_0| = 6$ then decreases, approaching asymptotically to ≈ 0.03 for $C_0/|T_0| > 20$.

In summary, the maximum $\Delta\tau/|T_0|$ and $\Delta\sigma/|T_0|$ errors are on the order of 4 to 5% of $|T_0|$, which lie within the usual allowable limits in any experimental approach and, therefore, are perfectly suitable for any conceivable engineering need.

Analysis of the dispersion of curve slopes also provides satisfactory results (see Fig. 11e). The maximum difference in angle β between the NGC and UC envelopes at the overlap zone is 4° for the case of $C_0/|T_0| = 5.8$, while it sharply approaches 0° for $C_0/|T_0| < 4$ and approaches asymptotically 2° for $C_0/|T_0| > 20$. It should be noted that the β angle is equivalent in practice to the instantaneous internal friction angle φ and that this is related to the α angle between σ_1 and fractures by the well known equation: $\alpha = 45° - \varphi/2$. Consequently, a 2 to 4° error in φ translates into a 1 to 2° error in the orientation of the fracture plane relative to the principal stress axis σ_1, which, for structural geologists, is also within the usual precision of compass measurements on natural fractures.

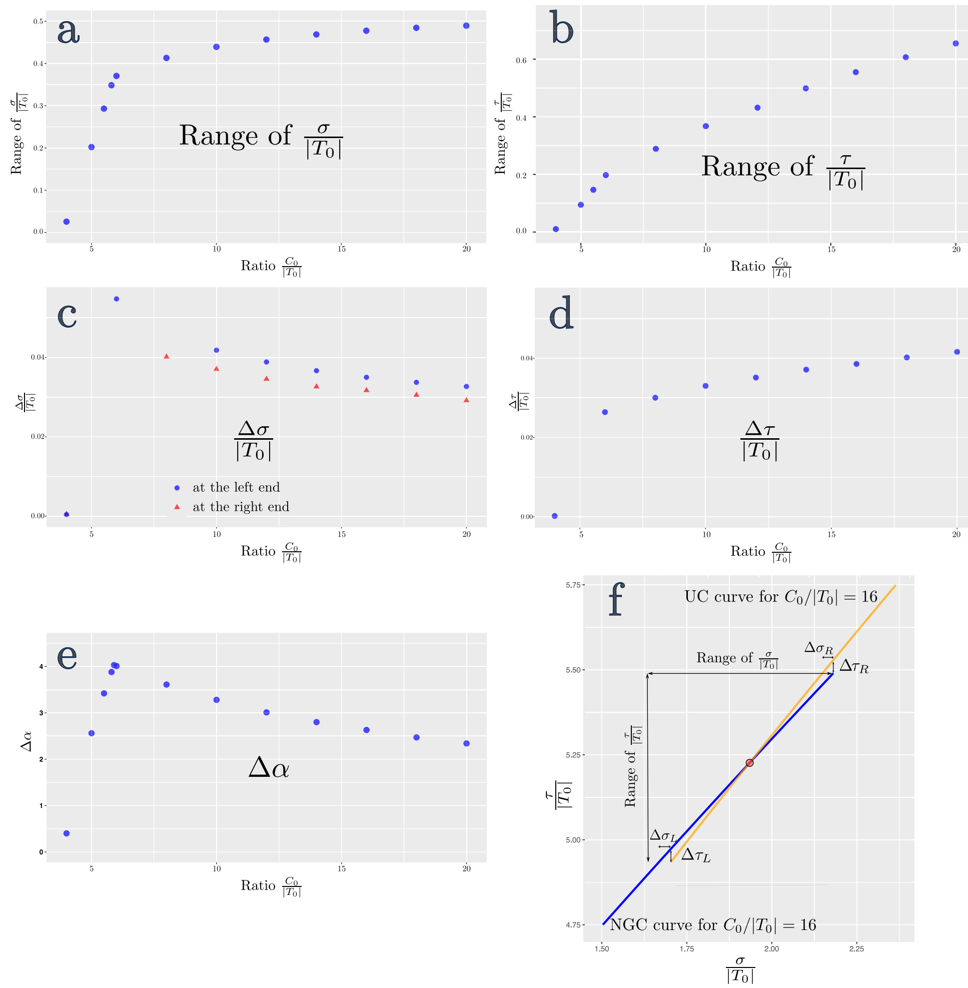

Fig. 11. Variation of the geometric elements of overlap of the NCG and UC curves for several ratios of $C_0/|T_0|$. (a) Variation of the overlap distance along the σ axis. (b) variation of the overlap distance along the τ axis. (c) Maximum uncertainty in sigma values between NGC and UC. (d) Maximum uncertainty in tau values between NGC and UC; both ends resulted symmetric. e: Maximum variation in α between NGC and UC. (f) geometric elements considered, for the case of ratio = 16.

7. Conclusions

In this work, we have revisited the classical Griffith criterion (OGC) in light of its known limitations and proposed a mathematically consistent modification (NGC) that improves its performance in the tensile and transitional regimes. We have also explored the compatibility of this modified formulation with Úcar's non-linear failure criterion (UC) for the compressive domain, thereby enabling the construction of a combined, virtually continuous failure envelope valid across the full stress spectrum—from pure tension to high confinement.

The formulation presented requires only the uniaxial compressive strength C_0 and tensile strength T_0 as input parameters (though it may benefit, of course, from a full set of triaxial tests). From these, it analytically derives all relevant components of the failure envelope. The new Griffith Criterion (NGC) retains the physical insight of the original Griffith approach while correcting its tendency to underestimate strength under compression. Úcar's Criterion (UC) (derived from a theorem of analytical geometry that states that if a family of involute curves admits a mathematical formulation, then a formula for the evolute can be obtained) complements the NGC by accurately capturing rock failure behaviour under compressive loading.

The combined NGC+UC envelope shows good agreement with a variety of experimental datasets, including confined extension and triaxial tests, and successfully reproduces both the magnitude and geometry of failure across the tensile, transitional, and compressive domains. This successful empirical verification fits our analysis of the errors at the overlap between the NGC and UC curves: these only reach 4 to 5% in σ and τ values, and 1 to 2° in the orientation of the fracture plane relative to the stress axes. This agreement, achieved despite the independent derivation of both criteria, underscores the robustness of the combined formulation and highlights its potential as a predictive tool in both academic and applied contexts.

Moreover, the mathematical nature of the formulation is well suited for implementation in numerical simulations. The simple examples provided here demonstrate its usefulness in the evaluation of fracture initiation thresholds under varying thermal, mechanical, and material conditions, showcasing its potential for offering valuable insights for subsurface tectonic and engineering problems. Taken together, the results suggest that the combined NGC+UC failure criterion provides a physically meaningful, computationally efficient, and empirically validated framework for modelling brittle failure in rocks. As such, it may serve as a valuable alternative to existing empirical criteria—particularly when data availability is limited to uniaxial test results.

Supplementary materials and code availability

The complete mathematical derivation of the proposed New Griffith Criterion (NGC), including the intermediate analytical developments omitted from the main manuscript, has been archived as a technical appendix in Zenodo as Úcar et al. (2026).

The complete R source code used to reproduce all examples and figures presented in this paper is openly available in a companion GitHub repository (Arlegui et al., 2026). The repository also contains the source code of the *NGC-Ucar Toolkit*, an interactive R Shiny application that allows users to:

- generate the combined NGC–Úcar failure envelopes from the uniaxial compressive and tensile strengths,
- visualise the envelopes in both the σ_n–τ and σ_3–σ_1 spaces,
- import and compare experimental triaxial test data with the theoretical failure envelopes, and
- export the calculated curves and associated parameter tables.

An online version of the application (that does not require any R installation on the user's machine) is freely accessible through Posit Connect Cloud at: https://luisarlegui-ngc-ucar-toolkit.share.connect.posit.cloud/

The Zenodo archive, GitHub repository and online application are cross-linked to facilitate reproducibility, transparency and long-term accessibility of the proposed methodology .

Symbol list	
NGC	New Griffith Criterion
OGC	Original Griffith Criterion
UC	Úcar Criterion
σ_1	Major effective principal stress
σ_3	Minor effective principal stress
$\overline{\sigma_1} = \sigma_1/C_0$	dimensionless major effective principal stress at failure
$\overline{\sigma_3} = \sigma_3/C_0$	dimensionless minor effective principal stress at failure
$\xi = T_0/C_0$	UC's main parameter
k_1, k_2, k_4	UC's parameters dependent on ξ
σ	effective normal stress
τ	shear stress
$C_o = \sigma_c$	Uniaxial compressive strength
$T_0 = \sigma_t$	tensile strength (always negative)
c	Cohesion
μ	Coefficient of internal friction
α	angle formed by the major principal stress with the failure plane
$\varphi = \varphi_i$	Instantaneous effective angle of internal friction ($\varphi_i = \beta$)
θ	angle between σ_1 and the normal to the plane of failure
β	slope of the envelope curve at any tangent
β_1, β_2, I	Parameters dependent on β_1 when $\sigma_3 = 0$ and β_2 when $\sigma = 0$
Ω	Parameter dependent on a
Ω_1	Integration constant
E	Elastic modulus
λ, a	Parameters for the NGC
ν	Poisson Coefficient
γ	Unit weight
α	Biot coefficient
Pf	piezometric height
Z	depth
TS	tectonic stress
α_t	Linear thermal expansion coefficient
σ_V	Vertical stress
σ_H	Horizontal stress
θ	angle between σ_1 and the normal to the failure plane.

CRediT authorship contribution statement

R. Úcar: Writing – original draft, Visualization, Methodology, Investigation, Formal analysis, Conceptualization. **L. Arlegui:** Writing – original draft, Visualization, Software, Investigation, Formal analysis, Data curation, Conceptualization. **N. Belandria:** Writing – original draft, Visualization, Software, Methodology, Investigation, Data curation, Conceptualization. **J.L. Simón:** Writing – original draft, Visualization, Formal analysis, Conceptualization.

Declaration of Generative AI and AI-assisted technologies in the writing process

During the preparation of this manuscript, the authors used DeepL and ChatGPT to improve the quality of the English language, not being native speakers. ChatGPT was also used to assist in debugging the R code. After using this tools, the authors reviewed and edited the content as needed and take full responsibility for the content of the published article.

Declaration of competing interest

The authors declare that they have no known competing financial interests or personal relationships that could have appeared to influence the work reported in this paper.

Acknowledgements

The authors wish to acknowledge the support from Gobierno de Aragón (Grant No. E32_26R Geotransfer Research Group) and European Union - Agencia Estatal de Investigación (Grant PID2023-148256NB-100 funded by MICIU/AEI/10.13039/501100011033 and by ERDF/EU).

Data availability

Data will be made available on request.

References

Anderson, E.M., 1951. The Dynamics of Faulting and Dyke Formation with Applications to Britain. Oliver & Boyd, Edimburgh, p. 206.

Arlegui, L., Simón, J., 2001. Geometry and distribution of regional joint sets in a non-homogeneous stress field: case study in the Ebro basin (Spain). J. Struct. Geol. 23 (2–3), 297–313. http://dx.doi.org/10.1016/S0191-8141(00)00097-3.

Arlegui, L.E., Úcar, R., Belandria, N., Simón, J.L., 2026. NGC-Ucar Toolkit. URL https://github.com/LuisArlegui/new_griffith_ucar_combined_failure_criterion.

Bahat, D., 1991. Tectonofractography. Springer, Heidelberg, http://dx.doi.org/10.1007/978-3-642-76162-1.

Baud, P., Wong, T.f., Zhu, W., 2014. Effects of porosity and crack density on the compressive strength of rocks. Int. J. Rock Mech. Min. Sci. 67, 202–211. http://dx.doi.org/10.1016/j.ijrmms.2013.08.031.

Belayneh, M., Cosgrove, J.W., 2010. Hybrid veins from the southern margin of the Bristol Channel Basin, UK. J. Struct. Geol. 32 (2), 192–201. http://dx.doi.org/10.1016/j.jsg.2009.11.010.

Bieniawski, Z., 1974. Estimating the strength of rock materials. J. South. Afr. Inst. Min. Met. 74 (8), 312–320.

Bobich, J.K., 2005. Experimental Analysis of the Extension to Shear Fracture Transition in Berea Sandstone (Ph.D. thesis). Texas A&M University.

Brace, W., 1960. An extension of the Griffith theory of fracture to rocks. J. Geophys. Res. 65 (10), 3477–3480.

Brace, W.F., 1964. Brittle fracture of rocks. In: State of Stress in the Earth's Crust. Elsevier.

Brace, W., Bombolakis, E., 1963. A note on brittle crack growth in compression. J. Geophys. Res. 68 (12), 3709–3713.

Brace, W., Paulding, Jr., B., Scholz, C., 1966. Dilatancy in the fracture of crystalline rocks. J. Geophys. Res. 71 (16), 3939–3953.

Castro, J., Cicero, S., Sagaseta, C., 2016. A criterion for brittle failure of rocks using the theory of critical distances. Rock Mech. Rock Eng. 49, 63–77.

Cordón, V., Arlegui, L., Simón, J.L., Toro, R., Úcar, R., Belandria, N., Torrijo, J., 2024. Úcar's non-linear rock failure criterion as a predictive tool and as a curve-fitting equation. In: Tomás, R., Cano, M., Riquelme, A., Pastor, J.L., Benavente, D., Ordóñez, S. (Eds.), New Challenges in Rock Mechanics and Rock Engineering, EUROCK 2024. ISRM European Rock Mechanics Symposium. CRC Press, London, http://dx.doi.org/10.1201/9781003429234.

Davis, G.H., Reynolds, S.J., Kluth, C.F., 2011. Structural Geology of Rocks and Regions. John Wiley & Sons, New York.

Drucker, D.C., Prager, W., 1952. Soil mechanics and plastic analysis or limit design. Quart. Appl. Math. 10 (2), 157–165.

Engelder, T., 1999. Transitional–tensile fracture propagation: a status report. J. Struct. Geol. 21 (8–9), 1049–1055. http://dx.doi.org/10.1016/S0191-8141(99)00023-1.

Etchecopar, A., Granier, T., Larroque, J., 1986. Origin of en echelon cracks-propagation of faults. C. R. l'Acad. Sci. Sér. II 302 (7), 479–484.

Etheridge, M., 1983. Differential stress magnitudes during regional deformation and metamorphism: upper bound imposed by tensile fracturing. Geology 11 (4), 231–234. http://dx.doi.org/10.1130/0091-7613(1983)11<231:DSMDRD>2.0.CO;2.

Fairhurst, C., 1964. On the validity of the 'Brazilian'test for brittle materials. In: International Journal of Rock Mechanics and Mining Sciences & Geomechanics Abstracts, vol. 1, (4), Elsevier, pp. 535–546.

Ferrill, D.A., McGinnis, R.N., Morris, A.P., Smart, K.J., 2012. Hybrid failure: Field evidence and influence on fault refraction. J. Struct. Geol. 42, 140–150. http://dx.doi.org/10.1016/j.jsg.2012.05.012.

Fossen, H., 2010. Structural geology. Cambridge University Press, p. 463.

Griffith, A.A., 1921. The phenomena of rupture and flow in solids. Philos. Trans. R. Soc. A: Math. Phys. Eng. Sci. 221 (582–593), 163–198.

Griffith, A.A., 1924. The theory of rupture. In: International Congress for Applied Mechanics. pp. 55–63.

Gudmundsson, A., 2011. Rock Fractures in Geological Processes. Cambridge University Press.

Hancock, P., 1985. Brittle microtectonics: principles and practice. J. Struct. Geol. 7 (3–4), 437–457. http://dx.doi.org/10.1016/0191-8141(85)90048-3.

Hancock, P., 1986. Joint spectra. In: Geology in the Real World-the Kingsley Dunham Volume. Dunham-Durham Reunion. pp. 155–164.

Hancock, P.L., Engelder, T., 1989. Neotectonic joints. Geol. Soc. Am. Bull. 101 (10), 1197–1208. http://dx.doi.org/10.1130/0016-7606(1989)101<1197:NJ>2.3.CO;2.

Hobbs, B., Means, P., 1976. An Outline of Structural Geology. Wiley & Sons, New York.

Hoek, E., 1965. Rock Fracture Under Static Stress Conditions. Technical Report, CSIR report MEG.

Hoek, E., 1983. Strength of jointed rock masses. Geotechnique 33 (3), 187–223.

Hoek, E., Brown, E., 1980. Empirical strength criterion for rock masses. J. Geotech. Eng. Div. 106 (9), 1013–1035. http://dx.doi.org/10.1680/geot.1983.33.3.187.

Hoek, E., Brown, E., 2019. The Hoek–Brown failure criterion and GSI –2018 edition. J. Rock Mech. Geotech. Eng. 11 (3), 445–463.

Hoek, E., Martin, C., 2014. Fracture initiation and propagation in intact rock – A review. J. Rock Mech. Geotech. Eng. 6 (4), 287–300. http://dx.doi.org/10.1016/j.jrmge.2014.06.001.

Horii, H., Nemat-Nasser, S., 1985. Compression-induced microcrack growth in brittle solids: Axial splitting and shear failure. J. Geophys. Res.: Solid Earth 90 (B4), 3105–3125. http://dx.doi.org/10.1029/JB090iB04p03105.

Irwin, G.R., 1963. Fracture by progressive crack extension. In: Proceedings of Symposium on Structural Dynamics under High Impulse Loading. In: Technical Documentary Report ASD-TDR-63-140, Aeronautical Systems Division, pp. 293–323.

Johnston, I.W., 1985. Strength of intact geomechanical materials. J. Geotech. Eng. 111 (6), 730–749. http://dx.doi.org/10.1061/(ASCE)0733-9410(1985)111:6(730).

Lan, H., Chen, J., Macciotta, R., 2019. Universal confined tensile strength of intact rock. Sci. Rep. 9 (1), 6170. http://dx.doi.org/10.1038/s41598-019-42698-6.

Leon, A., 1934. Über die Rolle des Trennbruches im Rahmen der mohrschen Anstrengungshypothese. Der Bauing. 31 (32), 318–321.

Mattauer, M., 1973. Les déformations des matériaux de l'écorce terrestre. In: Collection Méthodes, Hermann, Paris, p. 403.

McClintock, F., Walsh, J., 1962. Friction on Griffith cracks in rocks under pressure. In: 4th Int. Cong. Appl. Mech.. American Society of Mechanical Engineers, Berkeley, CA, pp. 1015–1021.

McCormick, C.A., Rutter, E.H., 2022. An experimental study of the transition from tensile failure to shear failure in Carrara marble and Solnhofen limestone: Does "hybrid failure" exist? Tectonophysics 844, 229623. http://dx.doi.org/10.1016/j.tecto.2022.229623.

Mogi, K., 1967. Effect of the intermediate principal stress on rock failure. J. Geophys. Res. 72 (20), 5117–5131. http://dx.doi.org/10.1029/JZ072i020p05117.

Muehlberger, W.R., 1961. Conjugate joint sets of small dihedral angle. J. Geol. 69 (2), 211–219. http://dx.doi.org/10.1086/626729.

Murrell, S., 1958. The strength of coal under triaxial compression. Mech. Prop. Non-Metallic Brittle Mater. 123–145.

Murrell, S., 1965. The effect of triaxial stress systems on the strength of rocks at atmospheric temperatures. Geophys. J. Int. 10 (3), 231–281.

Murrell, S., Digby, P., 1970. The theory of brittle fracture initiation under triaxial stress conditions—I. Geophys. J. Int. 19 (4), 309–334.

Nadai, A., 1950. Theory of Flow and Fracture of Solids, second ed. McGraw-Hill Book Co., New York.

Peacock, D., Sanderson, D.J., Leiss, B., 2021. Use of mohr diagrams to predict fracturing in a potential geothermal reservoir. Geosciences 11 (12), http://dx.doi.org/10.3390/geosciences11120501.

Peacock, D., Sanderson, D.J., Leiss, B., 2024. Use of Mohr diagrams to predict fracturing in rock masses, with applications for predicting sub-surface behavior. IScience 27 (8), http://dx.doi.org/10.1016/j.isci.2024.110272.

Peng, S., Johnson, A., 1972. Crack growth and faulting in cylindrical specimens of Chelmsford granite. In: International Journal of Rock Mechanics and Mining Sciences & Geomechanics Abstracts, vol. 9, (1), Elsevier, pp. 37–86. http://dx.doi.org/10.1016/0148-9062(72)90050-2.

Pollard, D.D., Aydin, A., 1988. Progress in understanding jointing over the past century. Geol. Soc. Am. Bull. 100 (8), 1181–1204. http://dx.doi.org/10.1130/0016-7606(1988)100<1181:PIUJOT>2.3.CO;2.

Pollard, D.D., Fletcher, R.C., 2005. Fundamentals of Structural Geology. Cambridge University Press.

Price, N.J., 1966. Fault and Joint Development in Brittle and Semi-Brittle Rock. Pergmon Press, New York.

Price, N.J., Cosgrove, J.W., 1990. Analysis of Geological Structures. Cambridge University Press.

Ramsey, J.M., Chester, F.M., 2004. Hybrid fracture and the transition from extension fracture to shear fracture. Nature 428 (6978), 63–66. http://dx.doi.org/10.1038/nature02333.

Reches, Z., Lockner, D.A., 1994. Nucleation and growth of faults in brittle rocks. J. Geophys. Res.: Solid Earth 99 (B9), 18159–18173. http://dx.doi.org/10.1029/94JB00115.

Reeher, L., Hughes, A., Davis, G., Kemeny, J., Ferrill, D., 2023. Finding the right place in Mohr circle space: Geologic evidence and implications for applying a non-linear failure criterion to fractured rock. J. Struct. Geol. 166, 104773. http://dx.doi.org/10.1016/j.jsg.2022.104773.

Scholz, C., 1968. Microfracturing and the inelastic deformation of rock in compression. J. Geophys. Res. 73 (4), 1417–1432.

Schultz, R., 2019. Geologic Fracture Mechanics. Cambridge University Press, Cambridge, England.

Segall, P., Pollard, D.D., 1983. Nucleation and growth of strike slip faults in granite. J. Geophys. Res.: Solid Earth 88 (B1), 555–568. http://dx.doi.org/10.1029/JB088iB01p00555.

Sibson, R.H., 1998. Brittle failure mode plots for compressional and extensional tectonic regimes. J. Struct. Geol. 20 (5), 655–660. http://dx.doi.org/10.1016/S0191-8141(98)00116-3.

Simón, J., Arlegui, L., Liesa, C., Maestro, A., 1999. Stress perturbations registered by jointing near strike-slip, normal, and reverse faults: Examples from the Ebro Basin, Spain. J. Geophys. Res.: Solid Earth 104 (B7), 15141–15153. http://dx.doi.org/10.1029/1998JB900070.

Simón, J., Arlegui, L., Pocovi, A., 2006. Fringe cracks and plumose structures in layered rocks: stepping senses and their implications for palaeostress interpretation. J. Struct. Geol. 28 (6), 1103–1113. http://dx.doi.org/10.1016/j.jsg.2006.03.015.

Suppe, J., 1985. Principles of Structural Geology. Prentice Hall, New Jersey, p. 537.

Tang, C., Hudson, J.A., 2010. Rock Failure Mechanisms: Explained and Illustrated. CRC Press.

Tapponnier, P., Brace, W., 1976. Development of stress-induced microcracks in Westerly granite. In: International Journal of Rock Mechanics and Mining Sciences & Geomechanics Abstracts, vol. 13, (4), Elsevier, pp. 103–112.

Tarokh, A., Sharpe, J.D., Labuz, J.F., 2022. Confined tensile testing of porous sandstone. Rock Mech. Rock Eng. 55, 6555–6566. http://dx.doi.org/10.1007/s00603-022-03007-2.

Taylor, D., 2008. The theory of critical distances. Eng. Fract. Mech. 75 (7), 1696–1705. http://dx.doi.org/10.1016/j.engfracmech.2007.04.007.

Twiss, R.J., Moores, E.M., 2007. Structural Geology, second ed. W. H. Freeman, New York.

Úcar, R., 1986. Determination of shear failure envelope in rock masses. J. Geotech. Eng. 112 (3), 303–315. http://dx.doi.org/10.1061/(ASCE)0733-9410(1986)112:3(303).

Úcar, R., 2021. Determination of a new failure criterion for rock mass and concrete. Geotech. Geol. Eng. 39 (5), 3795–3813. http://dx.doi.org/10.1007/s10706-021-01728-9.

Úcar, R., Arlegui, L., Belandria, N., Simón, J., 2026. A century after Griffith: Towards a combined non-linear criterion for brittle failure – technical appendix. http://dx.doi.org/10.5281/zenodo.21869784.

Úcar, R., Arlegui, L., Belandria, N., Torrijo, F., 2024. Estimating rock strength parameters across varied failure criteria: Application of spreadsheet and R-based orthogonal regression to triaxial test data. J. Rock Mech. Geotech. Eng. http://dx.doi.org/10.1016/j.jrmge.2024.11.024.

van der Pluijm, B., Marshak, S., 2004. Earth Structure: An Introduction to Structural Geology and Tectonics, second ed. W.W. Norton & Company, New York.

Wibberley, C.A., Petit, J.-P., Rives, T., 2000. Micromechanics of shear rupture and the control of normal stress. J. Struct. Geol. 22 (4), 411–427. http://dx.doi.org/10.1016/S0191-8141(99)00158-3.

Willemse, E.J., Pollard, D.D., 1998. On the orientation and patterns of wing cracks and solution surfaces at the tips of a sliding flaw or fault. J. Geophys. Res.: Solid Earth 103 (B2), 2427–2438. http://dx.doi.org/10.1029/97JB01587.